Methods for Determination of III-V Semiconductor Refractive Indices from Reflectance Interference Fringes

Samuel Davis, BSc (Hons)

Department of Physics

Lancaster University

A dissertation submitted for the degree of

Master of Science by Research in Physics

November, 2025

Methods for Determination of III-V Semiconductor Refractive Indices from Reflectance Interference Fringes

Samuel Davis, BSc (Hons).

Department of Physics, Lancaster University

A dissertation submitted for the degree of *Master of Science by Research*.

November, 2025.

Abstract

Accurate dispersive refractive indices for GaSb and AlAsSb are highly desirable for the design of GaSb-based resonant cavity devices operating in the 2-8 µm range. This dissertation reports on the development of two novel methods for the application of the well-known Swanepoel method in the case where normal incidence reflectance spectra are unavailable. By utilising linear regression of oblique angle reflectance spectra to determine normal incidence values, the required input data for the standard Swanepoel method can be calculated without direct measurement of normal incidence reflectance. Dispersive refractive indices calculated from this first method are shown to be in good agreement with literature data and are applied to the modelling of a DBR stopband, where they show significant improvement in agreement between modelled and measured reflectance when compared to experimental literature. The second method determines non-dispersive infrared refractive indices by a second-order Taylor expansion of Swanepoel's equations and is shown to be capable of predicting a reasonable trend in the refractive index of dilute $(\text{InAs}_{0.91}\text{Sb}_{0.09})_x\text{GaSb}_{1-x}$ alloy with increasing indium content.

Acknowledgements

I am exceptionally lucky to have had a great deal of support in my academic pursuits throughout my life, and I am quite pointedly aware that without that support this dissertation would certainly not exist. This dissertation is dedicated to my mum, Rachel, who has always shown unerring determination to provide me with the widest range of academic opportunities and support that she could, often in the face of significant challenges. I'm very lucky to be your son.

I owe a great debt of gratitude to my supervisor, Dr Andy Marshall, not only for the volume of wisdom and guidance provided throughout this year of study, but also for reigniting my interest in physics and giving me the push to pursue further study (whether that was intentional or not!). Without your level-headed advice, this work would have been one hell of a lot harder.

I cannot overstate the huge amount of support and sage guidance provided by each member of Andy's research group, and I am certain that without any one of them, this dissertation would not have turned out the way it has. Thank you in particular to Josh Fletcher, you have been an invaluable sounding board for experimental work, coding, and writing. I will never be able to repay the amount of time you have so kindly spent helping me.

Finally, outside of the scientific field, I would like to acknowledge my fantastic set of friends and my wonderful partner, Freya. To Freya, thank you for your wonderfully odd sense of humour with which you never miss a chance to raise my spirits, and for your unending patience for my shenanigans. To my friends in The Gap, I think you each know at this point how much you mean to me, and I am very lucky to know each of you so well. To all my friends and family not aforementioned, it is your influence that has made me the person I am today, and I am deeply grateful for all your support.

Declaration

I declare that the work presented in this dissertation is, to the best of my knowledge and belief, original and my own work. The material has not been submitted, either in whole or in part, for a degree at this, or any other university. This dissertation does not exceed the maximum permitted word length of 35,000 words excluding the bibliography and appendices. A rough estimate of the word count is: 9515

Samuel Davis

Publications and Presentations

Poster - S. Davis, A. Craig, J. Fletcher, G. Seager, K. Mamic, A. Marshall. *Methods for Determination of Refractive Index from Reflection Interference Fringes*. UK Semiconductors 2024, Sheffield Hallam University, July 2024.

Contents

List of Abbreviations

ADC   Analogue to Digital Converter

APM   Approximated Penn Model

DBR   Distributed Bragg Reflector

FTIR   Fourier Transform Infrared Spectrometer

FWHM   Full Width at Half Maximum

LED   Light-emitting Diode

MBE   Molecular Beam Epitaxy

MCE   Modified Cauchy Equation

MIR   Mid-infrared

NIR   Near-infrared

RHEED   Reflection High-Energy Electron Diffraction

SEM   Scanning Electron Microscopy

TMM   Transfer Matrix Method

XRD   X-ray Diffraction

List of Tables

List of Figures

Chapter 1

Introduction

Enhanced Q-factor and spectral selectivity are well-documented benefits of applying resonant cavity design to mid-infrared (MIR) photodetectors and LEDs [1]. In parallel, the GaSb material system, whilst not as well-studied as GaAs or InP, is increasingly used for MIR optoelectronics [2, 3, 4]. Cavity devices on GaSb in the 2-8 μm range frequently use GaSb/AlAsSb DBRs to form the optical cavity [5, 6, 7, 8]. The refractive indices of the materials that form the DBRs have significant influence on the properties of the DBR stopbands [9, 10], which are the primary factors in determining the operating wavelength of resonant cavity devices. Thus, to control the resonant wavelength of the final cavity-enhanced device, accurate refractive indices for the DBR layer materials are essential. Experimental refractive index data for GaSb and AlAsSb that covers the 2-8 μm range is lacking, particularly for AlAsSb [11, 12, 13].

Popular methods for the determination of refractive indices often rely on the use of spectroscopic ellipsometers [12, 14], the infrared variants of which can be prohibitively expensive for use in laboratories not focused on such applications. Furthermore, ellipsometry studies can be complicated by the need to prepare a clean surface on the sample [15], which would especially be a concern due to oxide formation on AlAsSb

epilayers.

An alternative method for dispersive refractive index characterisation was presented by R. Swanepoel based on the analysis of the interference fringes present in the reflectance spectra of coherent films [16]. This method models dispersion by observation of the change in the position of the interference fringe extrema between normal and oblique angles of incidence to the film. Whilst promising in its simplicity, this method requires a normal incidence reflectance spectrum for the film, which can pose an issue as many methods for measuring normal incidence reflectance are in fact at near-normal angles.

The aim of the work presented in this dissertation is the investigation of techniques to circumvent the Swanepoel method's reliance on normal incidence reflectance spectra. Chapter 2 provides the required background physics to understand the methods detailed later on and summarises existing refractive index data for GaSb, AlAsSb, and InGaAsSb. Chapter 3 describes the experimental procedures used to produce and analyse the epilayer samples used in this study. An analysis of those epilayers, including material quality and layer thicknesses, is detailed in Chapter 4. Chapter 5 describes a procedure for the use of the Swanepoel method on reflectance data collected at multiple oblique angles of incidence and then presents the dispersive refractive indices resulting from the application of this method to GaSb and AlAsSb. Additionally, these values are applied to the simulation of a DBR stopband, with comparison to experimentally measured reflectance. Chapter 6, the final results chapter, presents an alternative method for analysis of reflectance interference fringes best suited to estimations of non-dispersive refractive indices. That method is then applied to a selection of dilute $(InAs_{0.91}Sb_{0.09})_x GaSb_{1-x}$ epilayers, and the trend in refractive index with indium content is outlined.

Chapter 2

Background

The essential theory for understanding of later sections is contained herein. Only material which has been substantively involved in this work has been included so as to not reproduce lengthy standard derivations which are not the author's own work.

2.1 Interference Fringe Relations

Extrema in the reflectance spectra fringes produced by coherent films occur at well-defined wavelengths where the interference relation shown in Equation (2.1) is satisfied. The refractive index of the coherent film at some wavelength λ_i is given by n_i, d is the film thickness, r is the angle of refraction within the film, and m is any integer or half-integer [16].

$$2n_i d cos(r) = m\lambda_i \qquad (2.1)$$

This relation is shown to hold true in Figure 2.1 - as incident angle increases, and

3

cos(*r*) must therefore decrease, extrema with equal *m* are shown to shift towards shorter wavelengths.
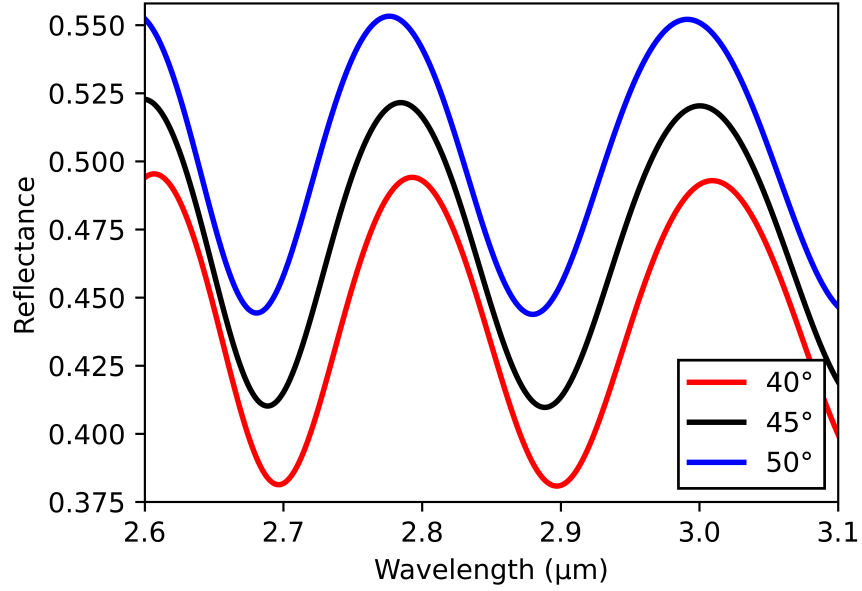
Figure 2.1: TMM simulation of a 5000 nm GaSb epilayer on GaAs at different angles of incidence. Literature values [11, 17] for the refractive indices are used.

For normal incidence reflection, Equation (2.1) simplifies to Equation (2.2), where the subscript 0 indicates the $0°$ angle of incidence specifically.

$$2n_0d = m\lambda_0 \tag{2.2}$$

2.2 The Swanepoel Method

Swanepoel presented a method for the determination of dispersive refractive indices by analysis of the wavelength positions of extrema in the interference fringes of

reflectance spectra. The method analyses coherent film interference extrema at both normal and an oblique angle (the case in the paper uses 30°) to determine the fitting parameters of the modified Cauchy equation (MCE) shown in Equation (2.3) [16].

$$n^2 = \frac{a}{\lambda^x} + b \qquad (2.3)$$

The MCE relates the dispersive refractive index (n) of a material to the wavelength (λ) using fitting parameters a, b, and x. It is a two term approximation of the Cauchy equation [18], which is shown in Equation (2.4) for completeness. A, B, and C are the fitting constants; n and λ are as defined above.

$$n = A + \frac{B}{\lambda^2} + \frac{C}{\lambda^4} + ... \qquad (2.4)$$

A key advantage of the Swanepoel method is that so long as the reflectance values of the studied spectra are well-defined enough for interference fringes to be visible, it does not rely on the reflectance values of the extrema beyond that, only on the wavelengths at which they occur. An ancillary benefit of the Swanepoel method is that it also returns an estimate for the thickness of the film causing the interference fringes, meaning it can be applied to verify other measurements or expectations of that value.

The Swanepoel method is used across a wide range of material systems [19, 20, 21], and efforts have been made to improve the method's performance in both transparent and high-absorption regions [22, 23]. For this work, however, the original method is used due to its computational simplicity.

2.3   Refractive Index and Optical Bandgap Relations

The Moss Relation [24], shown in Equation (2.5), empirically relates the optical bandgap (E_g) and the non-dispersive refractive index (n) of a material.

$$n^4 E_g = M \tag{2.5}$$

In the original Moss relation, M is stated to be 95 eV. A similar relation was later developed specifically for use with semiconductors by consideration of the Penn model [25] of dielectric constants, giving the approximated Penn model (APM) shown in Equation (2.6) [26].

$$n = 4.16 - AE_g + BE_g{}^2 - CE_g{}^3 \tag{2.6}$$

Coefficients A, B, and C are 1.12 eV^{-1}, 0.31 eV^{-2}, and 0.08 eV^{-3} respectively. The coefficients used in this model were determined via consideration of the relation between the Penn gap and the bandgap of a wide range of semiconducting materials. The model predicts non-dispersive refractive indices well, but it is evident from the data presented in Gupta's work that it tends to underestimate values for gallium-rich compounds.

2.4   Distributed Bragg Reflectors

Distributed Bragg Reflectors (DBRs) are fundamental structures to the development of optical cavities as they can be designed to have very high reflectance for only a specific section of the wavelength spectrum. A DBR consists of alternating layers

of high and low refractive index materials, each of which must have an appropriate optical path length to achieve constructive interference in the reflected component. This is typically achieved by each layer having optical path length equal to one-quarter of the target wavelength (λ_t) for the structure.

When incident light transitions from a low refractive index to a high refractive index at a boundary between contrasting layers, the reflected component of that light undergoes a π rad phase shift. For light with wavelength close to λ_t, each interface's reflected light is separated by a half-wavelength optical path length, and will interfere constructively due to the phase shift. This constructive interference between the reflected light significantly increases the structure's reflectance. That constructive interference will not occur consistently for light that is not near the target wavelength as the reflected and incoming light will not be in phase. This leads to a spectrally narrow region of high reflectance called the stopband.

Assuming that incoming light is at normal incidence and there is no absorption in a DBR, the width ($\Delta\lambda$) and peak reflectance (R) of its stopband can be determined by Equation (2.7) [9] and Equation (2.8) [10] respectively.

$$\Delta\lambda \approx \frac{4\lambda_t}{\pi} arcsin\left(\frac{n_H - n_L}{n_H + n_L}\right) \tag{2.7}$$

$$R = \left(\frac{n_0 n_L{}^{2N} - n_s n_H{}^{2N}}{n_0 n_L{}^{2N} + n_s n_H{}^{2N}}\right)^2 \tag{2.8}$$

The refractive indices of the originating medium, substrate, high refractive index material, and low refractive index material are indicated by n_0, n_s, n_H, and n_L respectively. N indicates the number of pairs of contrasting layers in the DBR. It is clear that the refractive indices of the DBR layers are of high impact on the shape of the stopband, which in turn will determine the spectral selectivity of devices utilising the DBR.
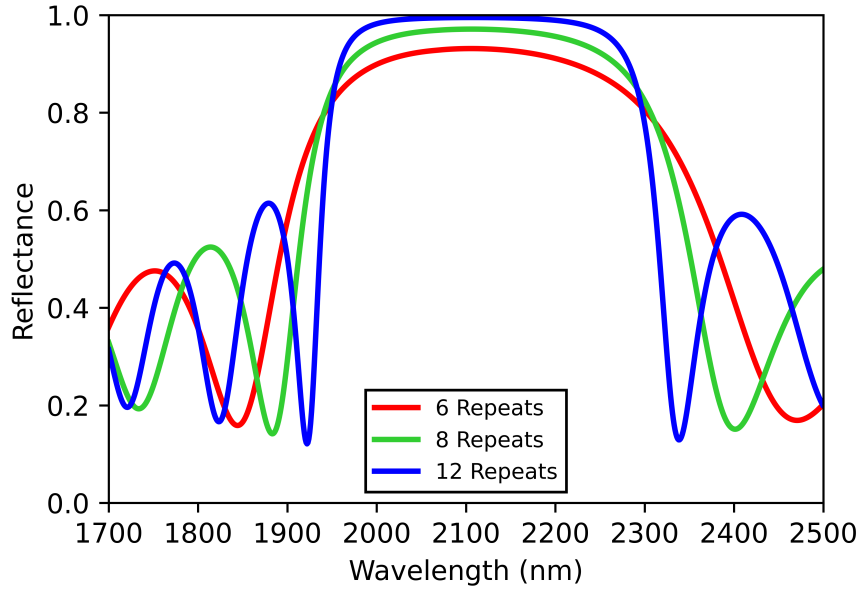
Figure 2.2: Reflectance spectra of 3 different GaSb/AlAsSb DBRs with increasing numbers of repeats modelled using a TMM model. Literature values [12, 13] for the refractive indices are used.

In Figure 2.2, example GaSb/AlAsSb DBRs are modelled using the TMM implementation described in Section 2.5. The AlAsSb layers are modelled with a non-dispersive refractive index of 3.1 [13] and a thickness of 169 nm, whilst the GaSb layers are 137 nm thick and their dispersive refractive index is taken from [12]. As predicted by Equation (2.8), the peak reflectance of the stopband can be seen to increase as the number of repeats in the DBR does.

2.5   Reflectance Modelling

Reflectance modelling was performed using the transfer matrix method (TMM), implemented in Python using the `tmm` package [27]. The model considers matrix

transformations of an electric field as it passes through a structure consisting of an arbitrary number of coherent films, which is bounded by two semi-infinite media. By combination of the transfer matrices applied to the electric field at each interface, the overall transfer matrix for the structure may be determined, and thus the reflectance may be retrieved [28].

Python functions were written to allow for the formation of reflectance spectra of arbitrary structures across a configurable wavelength range. As the `tmm` function needed to be run at each wavelength, a looping wrapper function was developed to automatically generate data for the reflectance plots. The input data for this function required basic details such as layer thicknesses and refractive indices, the latter of which were primarily sourced from literature [11, 12, 13, 17] or the characterisation undertaken in this work. It was assumed during these simulations that the absorption coefficients of the materials forming the coherent layers were negligible as the `tmm.tmm_core.coh_tmm` function assumes no absorption is present in the stack. The wavelength range for this study has been selected not only for relevance to potential applications but also to ensure the above assumption is valid.

Examples of this TMM implementation producing expected results are shown in Figures 2.1 and 2.2. Matplotlib [29] was used for plotting in the aforementioned figures and throughout the rest of this dissertation.

2.6 Existing Refractive Index Data

As mentioned in Chapter 1, existing experimental refractive index data for both GaSb and AlAsSb fails to cover the entirety of the 2-8 μm range. In particular, there is no experimentally-based reference data for AlAsSb lattice-matched to GaSb anywhere in this work's spectral range. For this reason, photothermal deflection spectroscopy

work by Saadallah that only covers up to 1.8 µm [13] is considered as a reference point. In addition, simulation work by Adachi that extends up to 6.2 µm [30] is used in later comparisons.

For GaSb, far more reference data is available: Roux's M-lines method returns data in the 2.15-7.35 µm range [11]; Munoz's ellipsometric study covers up to 4.1 µm [14]; and Ferrini's ellipsometry work presents data up to 2.48 µm [12]. Munoz also provides values for InGaAsSb with 15 and 16% In, although the experimental methodology is somewhat unclear [15]. Data for all of the literature studies was extracted from the published dispersion curves.

Chapter 3

Methodology

The essential experimental methods utilised in this body of work are detailed herein, including sample production, composition analysis, and both normal and oblique angle reflectance measurements.

3.1 Layer Thickness in Molecular Beam Epitaxy

Samples for this study were grown in-house by molecular beam epitaxy (MBE) using a Veeco GENXplor solid source reactor. The details of the procedures involved are beyond the scope of this dissertation as the sample growth itself was not performed by the author. Instead, some consideration must be lent to the accuracy to which the thickness of MBE-grown layers can be known without additional measurements.

Growth rates for each source are calibrated after each maintenance cycle by observation of reflection high-energy electron diffraction (RHEED) oscillations and repeated occasionally during each 6-12 month growth campaign. By combination of the target lattice constant, the growth rate, and the growth time, an estimate of the

total thickness of any given layer in a structure may be determined. Assuming that the material growth is group-III limited, the uncertainty in the nominal thickness will primarily be due to fluctuations in the group-III growth rate.

Barring the InGaAsSb epilayers, all samples involved in this study were grown from the same set of calibrations. Aluminium growth rates are expected to be lower than the nominal value as the only available calibration for this source was the one performed immediately after replacement when the melting process had only just occurred, leading to higher Al flux at the time of calibration. Unlike the Aluminium source, the Gallium source is not replaced during maintenance periods. Across a number of years its growth rate has been measured to remain approximately constant, without a discernible time or usage dependent drift, hence the Ga rate is expected to fluctuate evenly around the nominal value by up to 5%.

3.2   X-Ray Diffraction

X-ray diffraction (XRD) measurements were used to study the lattice constants of the epitaxially grown structures. When x-rays are incident upon a crystal lattice, they will scatter due to interactions with atomic electrons, and these scattered x-rays will interfere constructively with each other at specific angles. Bragg's law (Equation (3.1)) describes the angles at which this interference occurs.

$$2dsin(\theta_B) = n\lambda \tag{3.1}$$

The angles of constructive interference are called Bragg angles (θ_B), and are related to the x-ray wavelength (λ), the order of diffraction (n), and the atomic plane spacing (d).

To find the Bragg angles, a coupled scan of the source-sample angle (ω) and the source-detector angle (2θ) is performed, with intensity peaks found when θ is a Bragg angle. During the scan, the angles are varied simultaneously with the constraint that ω must always be equal to θ. This $\omega - 2\theta$ scan is preceded by a series of calibrations that optimise the horizontal position of the sample, locate the zero point of ω, and find the peak intensity values for each of ω, 2θ, and the wafer holder angle.

A Bruker D8 Discover is used to perform the $\omega - 2\theta$ scan, and the resulting spectrum provides information about the Bragg angle for each material in the structure. The height of the peaks correlates to both the thickness of each layer and the layer's depth below the surface of the structure, so the substrate will often cause a high-intensity peak despite being the deepest layer.
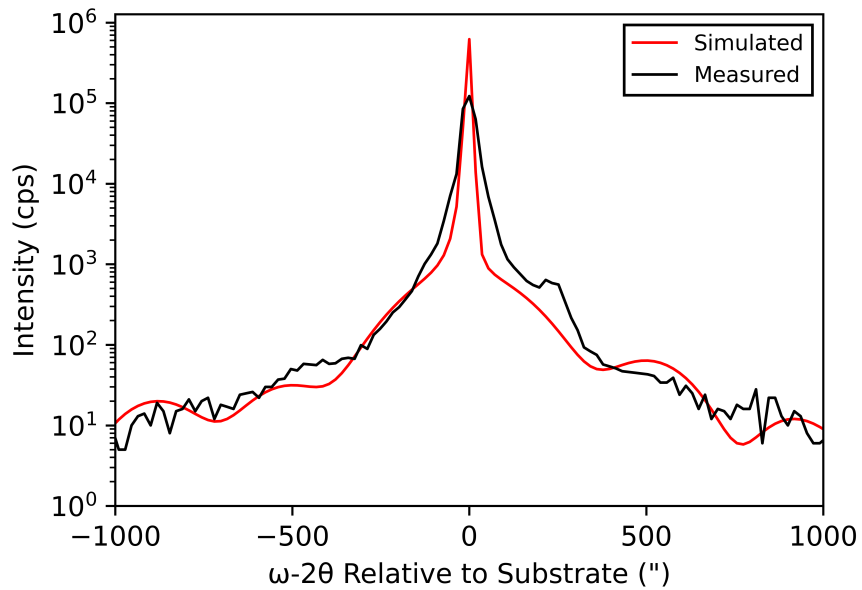
Figure 3.1: XRD measurement of an AlAsSb calibration epilayer grown on GaSb.

To analyse the spectra, Bede RADS software was used to simulate XRD patterns for arbitrary structures, and the comparison between the simulated and measured

spectra was used to determine the composition of the epilayers in the structure. The example spectrum shown in Figure 3.1 only shows a single peak, indicating an excellent lattice match between the AlAsSb epilayer and the GaSb substrate. The FWHM of the peak is only 40", implying very good material quality.

3.3   Variable Angle Optical Reflectance Measurements

The core apparatus for the measurement of reflectance at a range of angles was a Bruker VERTEX 70 FTIR outfitted with a PIKE Technologies VeeMAX III variable angle reflection accessory.

The experimental apparatus for the measurement of variable angle reflectance spectra (Figure 3.2) functions as follows: the globar (silicon carbide) source (1) emits MIR radiation that is reflected off the parabolic source mirror (2) before passing through the aperture wheel (3) and filter wheel (4). The beam is collimated by the interferometer entrance mirror (5), split by the KBr beam splitter (a partial reflector, 6) and then reflected back to the beamsplitter by two adjustable plane mirrors (7 & 8). Having passed through the interferometer, the beam is reflected off the parabolic sample compartment mirror (9) and passes through the VeeMAX III variable angle reflectance accessory (11, see Figure 3.3). Upon exiting the variable reflector, the light is incident upon the parabolic detector mirror (12) and is focused upon the DLaTGS internal detector (13).

The differing path lengths between the two mobile plane mirrors and the beamsplitter in the interferometer cause interference in the combined beam, resulting in a time dependency in the detector signal. The interferogram created by the sampling of the time-dependent detector signal at multiple points undergoes a Fourier transform to produce a high-resolution ($\sim$4cm^{-1}) reflectance spectrum. To ensure the resultant
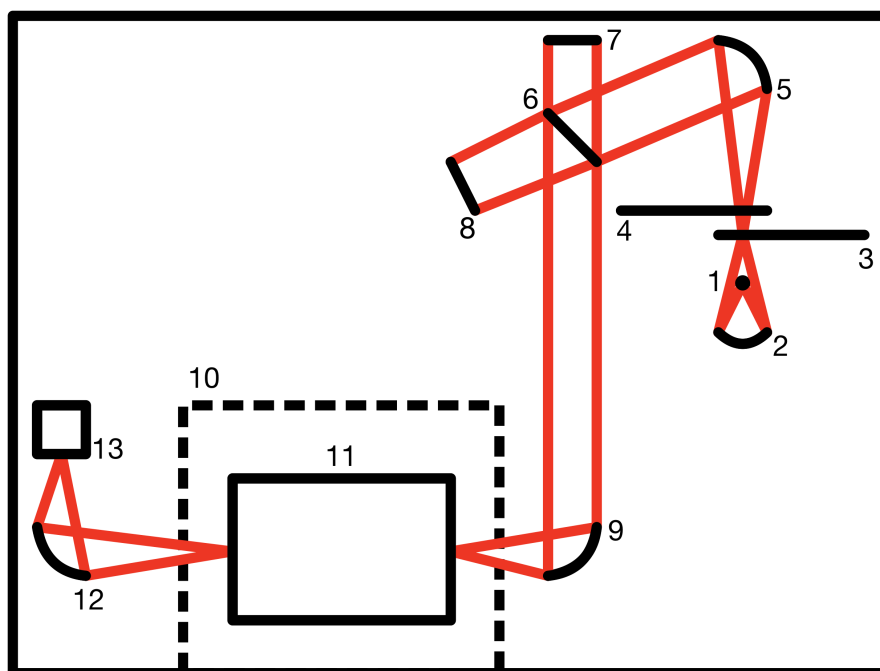
Figure 3.2: Beampath diagram for variable angle reflectance measurements using the FTIR's sample compartment. 1. Globar (silicon carbide) MIR Source 2. Source mirror 3. Aperture wheel 4. Filter wheel 5. Interferometer entrance mirror 6. KBr beam splitter 7. Moving plane mirror 8. Moving plane mirror 9. Sample compartment mirror 10. Sample compartment boundary 11. VeeMAX III variable angle reflectance accessory 12. Detector mirror 13. DLaTGS detector.

reflectance spectra accounted only for the reflection from the sample placed on the variable reflector, a background measurement using a highly reflective gold mirror preceded each set of sample measurements. This background spectrum was then used by the OPUS software to calculate the reflectance spectra of the sample (by dividing the sample scan by the background scan).

Light passing through the variable reflector (shown in Figure 3.3) undergoes the following process: it is reflected by a beam steering mirror (1) and then a plane mirror
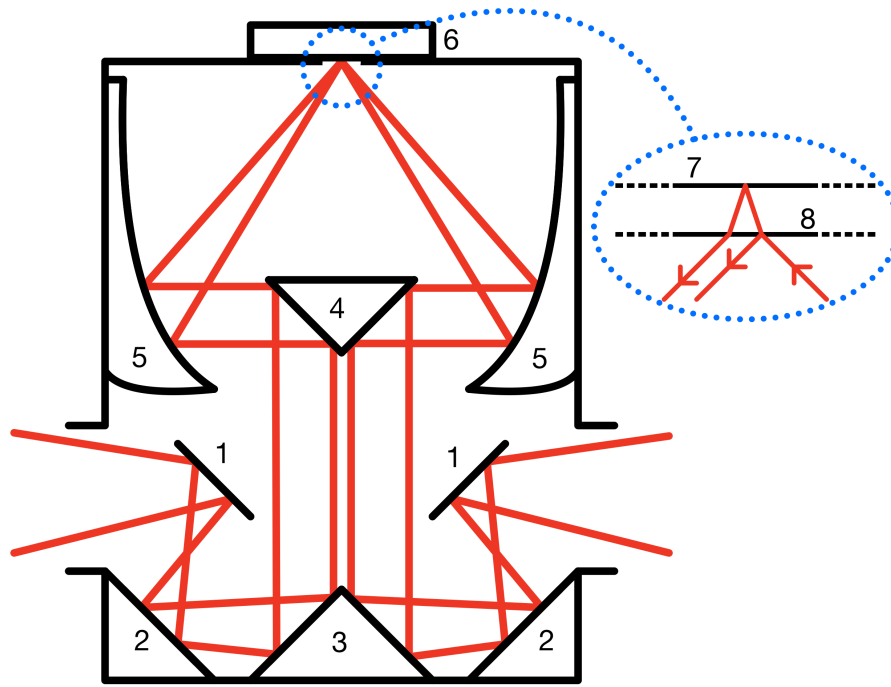
Figure 3.3: Simplified beam path diagram for the PIKE VeeMAX III variable angle reflectance accessory. 1. Beam steering mirrors 2. Plane mirrors 3. Parabolic collimating mirror 4. Vertical adjustable mirror 5. Large parabolic mirrors 6. Sample 7. Substrate-epilayer interface 8. Epilayer-air interface.

(2) onto a parabolic collimating mirror (3). The collimated beam is then incident upon the vertically adjustable mirror (4), which reflects it onto one of the large parabolic mirrors (5). The large parabolic mirror directs the beam to be incident upon the sample (6) in a loosely focused spot. At the sample, the beam undergoes two relevant reflections: one from the epilayer-air interface (8), and one from the substrate-epilayer interface (7). The reflected light from the two interfaces has a small path length difference, leading to interference in the reflected beam. The steps involving components 1 through 6 are then repeated in reverse for the reflected beam.

The angle at which the beam is incident upon the sample is determined by the vertical

position of the adjustable mirror (4). The angle may be set between 30° and 80°, but the overall transmission of the variable reflector is at its maximum between 45° and 50°, with significant fall-off outside of that range. That fall-off is not a significant concern when variable angle reflectance spectra are used in the Swanepoel method, as the method is broadly insensitive to the magnitude of the reflectance.

The VeeMAX III is supplied with three masks of varying sizes to allow for controlled areas of samples to be studied. The masks are machined and coated to be non-reflective, although as this is not perfectly effective, the aperture of the FTIR beam should be carefully limited to minimise stray reflections from the underside of the mask. These reflections can be especially prominent at high angles of incidence, where the beam spot on the sample becomes increasingly elliptical. In this study it was determined that the largest mask that the sample and mirror both completely cover should be used, and the same mask should be used for both the sample and gold mirror. This is to ensure that the reflectance of the sample is not unnecessarily suppressed, as severe suppression can lead to difficulties identifying fringe extrema.

Reflectance spectra for a GaSb epilayer at varying angles of incidence measured using the described apparatus and methodology are presented in Figure 3.4. In comparison to the simulated reflectance spectra, the period of the fringes can be seen to be very similar, with the slight offset in spectral position and small period difference most likely being due to a slight difference in the GaSb epilayer thickness between the simulation and sample.

A significant problem for the use of variable angle reflectance spectra measured with the above technique in the Swanepoel method is the presence of atmospheric absorption extrema, particularly CO_2 at 4.2 µm. As the Swanepoel method requires continuous extrema, and the peak-finding algorithm used to analyse the reflectance spectra could not distinguish between atmospheric absorption extrema and inter-ference fringe extrema, the wavelength range analysed was limited to 2-4.15 µm.
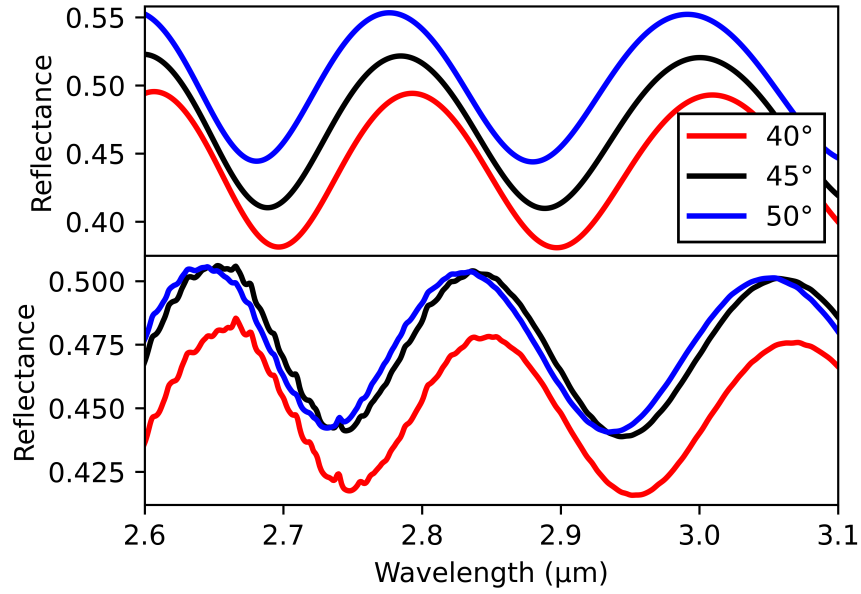
Figure 3.4: Experimental reflectance spectra (bottom) for a ∼5000 nm GaSb on GaAs epilayer compared to the simulated reflectance spectra (top) from Figure 2.1.

However, beyond the CO_2 peak, GaSb and AlAsSb are expected to have very low dispersion [11, 30], so this limited range of study was not considered an obstacle to presenting data over the 2-8 μm range.

3.3.1   Angular Resolution

By consideration of the resolution of the angular scale on the variable reflector, its angular uncertainty was initially estimated to be 0.5°. To form a more comprehensive uncertainty estimate, the reflectance of a GaAs substrate to p-polarised light was measured across the angular range of the reflector. This was then used to compare the angle at which minimum reflectance occurs in the measured reflectance spectrum to the Brewster's angle of GaAs, which was calculated from literature data [17].

To avoid the lengthy process of sample and background scanning at each angle, the reflectance was approximated by recording the ADC counts (a ratiometric voltage value) of the FTIR's analogue-to-digital converter (ADC) for each of the GaAs substrate and gold mirror in 1° steps across the range. By taking the ratio of these ADC counts, the average reflectance of the GaAs substrate across the FTIR's spectral range was determined. The validity of the ADC count approach for approximating reflectance can be confirmed by considering that GaAs has little dispersion in the wavelength range studied [17], so reflectance and its associated properties would be expected to function more strongly as a function of incident angle rather than wavelength.
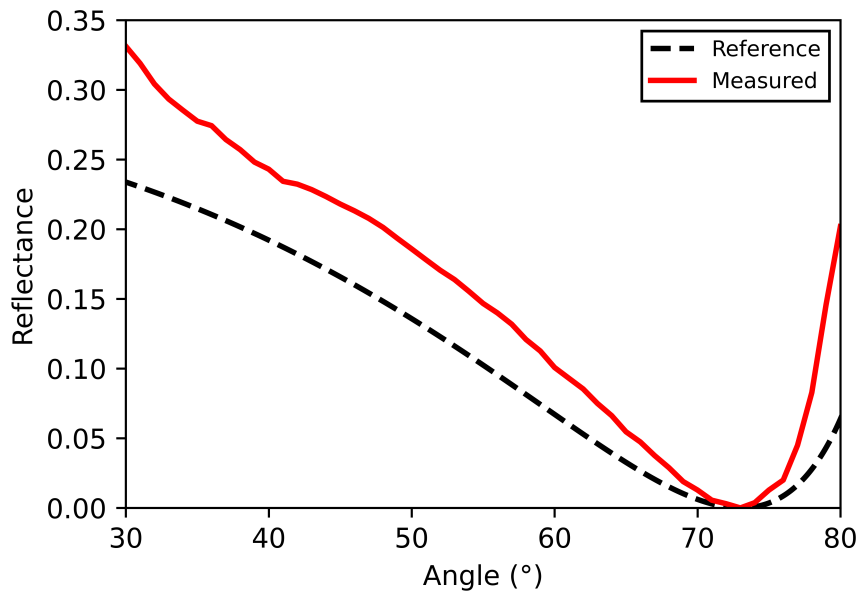
Figure 3.5: Reflectance of p-polarised light on GaAs at varying angles of incidence. The reference line uses literature data [17].

The reflectance of GaAs to p-polarised light at varying angles of incidence is presented in Figure 3.5. The reflectance was corrected by taking the minimum value in the GaAs ADC counts to be equal to zero reflectance, and then correcting the

rest of the ADC values by that offset. This correction is reasonable in the measured range, as by the definition of Brewster's angle, the minimum reflectance value must be equal to zero. The reference curve was calculated using Fresnel equations with literature data [17] for the refractive index of GaAs. Given that the reference curve and measured reflectance minimas are both located at $73°$, the angular uncertainty for the variable reflector was confirmed to be $0.5°$, primarily deriving for the resolution of its angular scale.

3.3.2   Background Considerations

As the Swanepoel method does not rely on a precise measurement of the reflectance of the interference fringe extrema, only their spectral position, some leeway is afforded in the selection of the background measurement used in measuring reflectance. In the interest of time efficiency, it is preferable to take a single background scan that is valid for all angles of incidence, rather than a background scan at each studied angle of incidence; the former option offers time savings of just under 50%.

To confirm that the angle of incidence at which the gold background was measured would not affect the positions of the fringe extrema, the reflectance of a GaSb epilayer was calculated using gold backgrounds measured at a small range of angles.

A section of each of the measured reflectance spectra of a GaSb epilayer is presented in Figure 3.6. The reflectance axis has been min-max scaled to normalise each data series to vary between 0 and 1 in order to enable direct comparison of fringe extremum positions. It can be clearly seen that the angle at which the gold background for a measurement is taken has no appreciable impact on the extremum positions in the reflectance interference fringes.
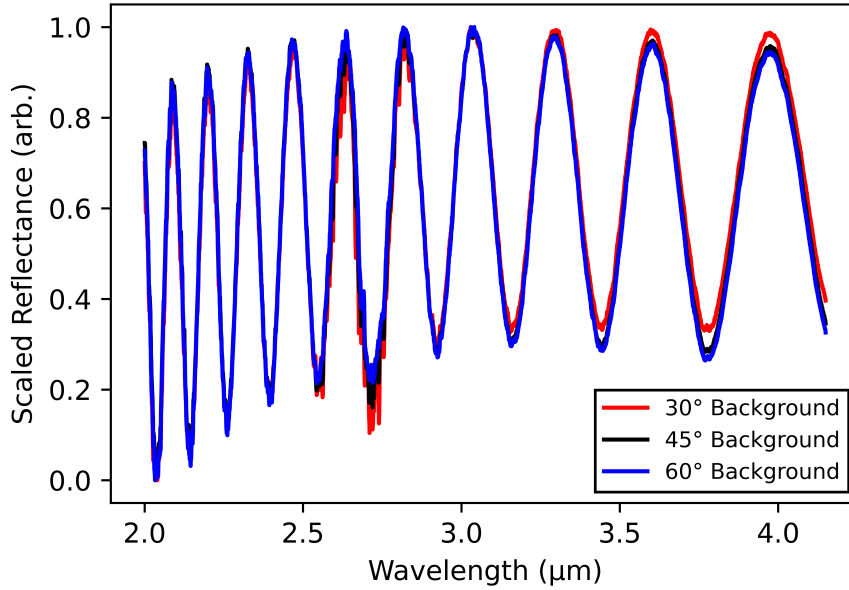
Figure 3.6: Min-max scaled reflectance spectra of a GaSb epilayer at varied angles of incidence.

3.3.3 Scan Duration

It was observed that due to time-dependent fluctuations in the local atmospheric composition, distortions in measured reflectance spectra from atmospheric absorption increased as the time between the background and sample scans increased. This was particularly problematic for water absorption noise around 2.6 µm as, in some cases, the noise in the reflectance spectra affected the apparent position of fringe extrema.

As a result, a trade-off in scan duration evolved: a lower number of scans (hence quicker measurements) led to increased noise across the spectrum but limited the effects of atmospheric absorption, whereas more scans (hence longer measurement times) suppressed noise in the spectra but caused noise deriving from atmospheric

absorption to become far more prominent. During this work, it was determined that for the specific experimental setup used, measurement durations of around 16 seconds provided the best trade-off between noise suppression, absorption peaks and time efficiency.

3.4   Normal Incidence Reflectance Measurements

To measure the reflectance of DBRs, normal incidence apparatus, which used the same FTIR as the variable reflectance setup, was used. The experimental apparatus (pictured in Figure 3.7) functions as follows: the tungsten halogen lamp source (1) emits NIR radiation that is reflected off the parabolic source mirror (2) before passing through the aperture wheel (3) and filter wheel (4). This beam is collimated by the interferometer entrance mirror (5), split by the partial reflection of the CaF$_2$ beam splitter (6), and then reflected by two adjustable plane mirrors (7 & 8) back through the beamsplitter. Having passed through the interferometer, the beam is then reflected off the channel mirror (9) to send it out of the FTIR and onto the periscope (10), which directs the beam onto the fibre entry parabolic mirror (11) where it is focused onto the SMA connector (12) for the inbound leg of the THORLABS BF19Y2LS02 bifurcated fibre (13). The fibre then joins the combined leg (14) and is directed toward the sample measurement area (15, see inset). In the sample measurement area (15, blue dotted inset), a clamp (18) mounted to an X-Y adjustable stage (20) holds the fibre (14) perpendicular to the sample and sample stage (19). Light exits the fibres of the inbound leg, reflects off the sample, and enters the fibres comprising the outbound leg (16). The light exits the outbound leg of the fibre and is incident upon the THORLABS PDA10D-EC amplified InGaAs detector (17). The signal from the detector is then sent through an additional amplifier and into the FTIR's analogue-to-digital converter.
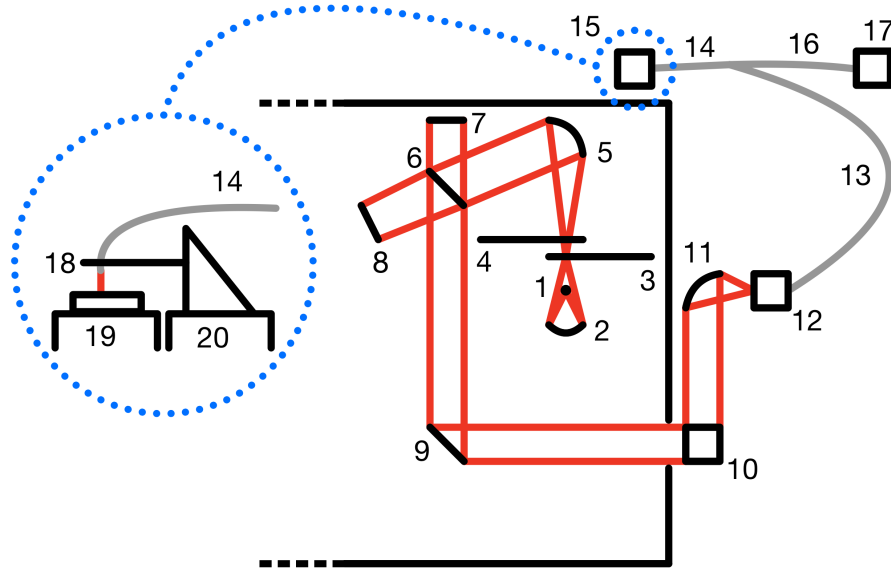
Figure 3.7: Beampath diagram for normal incidence reflectance measurements using an external detector. 1. Tungsten halogen lamp NIR source 2. Source mirror 3. Aperture wheel 4. Filter wheel 5. Interferometer entrance mirror 6. CaF$_2$ beam splitter 7. Moving plane mirror 8. Moving plane mirror 9. Channel mirror 10. Periscope mirror 11. Fibre entry parabolic mirror 12. Fibre inbound leg SMA connector mounting point 13. Fibre inbound leg 14. Fibre combined leg 15. Sample stage 16. Fibre outbound leg 17. THORLABS amplified InGaAs detector 18. Clamp holding fibre combined leg SMA connector 19. Sample stage 20. X-Y adjustable stage.

As with variable angle reflectance measurements (Section 3.3), each sample measurement was preceded by a scan of a high reflectivity gold mirror, which was then used by the OPUS software to calculate reflectance. The distance between the sample and the fibre exit was optimised before each sample measurement to ensure the maximum possible signal reached the InGaAs detector. The primary limitation of this experimental setup was the short cutoff wavelength (2400 nm) of the BF19Y2LS02 fibre, which made the apparatus unsuitable for the measurement of reflectance interference fringes, hence motivating much of the work to circumvent

the Swanepoel method's reliance on normal reflectance spectra. However, this setup was utilised for the measurement of DBR reflectance spectra to compare stopband properties between TMM modelling and experiment.

Chapter 4

Results I: Sample Analysis

The MBE-grown samples used for this study are detailed herein. The thick epilayers grown for this work were each grown to a target thickness of 5000 nm in order to increase fringe density and ensure there were a large number of extrema present in the studied wavelength range.

4.1   GaSb Epilayer

GA1, the GaSb epilayer, was grown metamorphically on undoped GaAs.   The thickness of this epilayer can be estimated to be 5130±50 nm from the SEM image in Figure 4.1. The uncertainty in this measurement, as with further measurements from SEM images described below, was estimated to be the standard error in a dataset of three thickness measurements taken from separate parts of the image. The imaging shows high film uniformity has been achieved, as is expected from MBE. Swanepoel analysis of its reflectance spectra indicates a thickness of 5030±70 nm, agreeing well with the SEM value.

Figure 4.1: Backscatter electron microscopy image of GA1, the GaSb epilayer. Growth direction is left to right. The thickness of the GaSb epilayer is 5130±50 nm.

The XRD pattern in Figure 4.2 shows a FWHM of 64" for the GaSb peak, which is at a position of -9600". These values are comparable with literature [31], and indicate good material quality, as is expected in the relatively simple case of metamorphic binary growth by MBE.

4.2   AlAsSb Epilayer 1

AL1, the first AlAsSb epilayer, was grown pseudomorphically on p-doped GaSb. Its growth was proceeded by the growth of a 1 µm thick calibration epilayer, the XRD
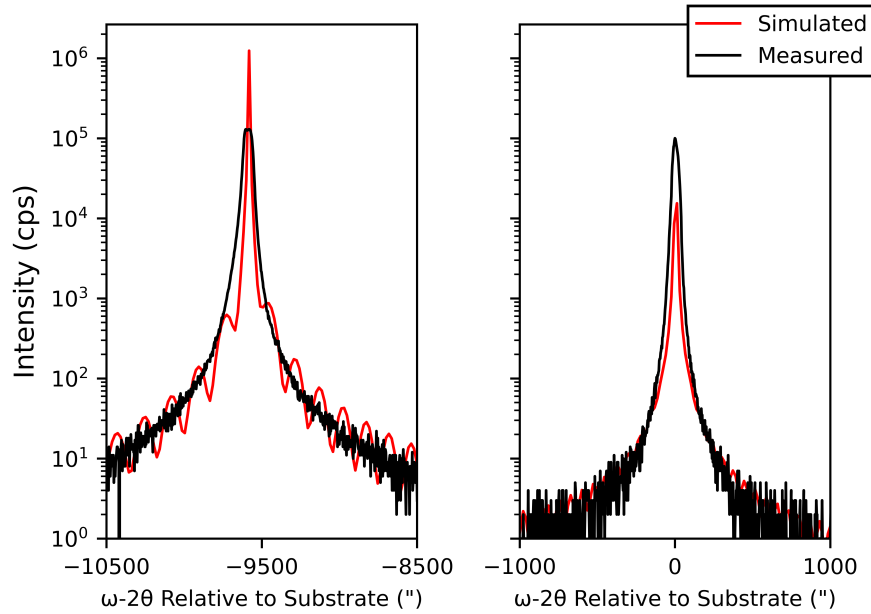
Figure 4.2: XRD Pattern of GA1, the GaSb epilayer. The left peak is the GaSb epilayer, the right peak is the GaAs substrate.

pattern of which is shown in Figure 3.1. Although the calibration epilayer exhibited excellent lattice matching between the AlAsSb and GaSb layers, this did not translate to AL1. To prevent oxidation, as with the calibration layer, AL1 was grown with a 50 nm GaSb cap, but this was etched down to a thickness of approximately 18 nm using citric acid. The cap etch was performed in order to minimise the effect that the presence of the cap would have upon AL1's reflectance spectra.

The thickness estimate of AL1 taken from the SEM image in Figure 4.3 is 4710$\pm$60 nm, which is notably thinner than the target thickness of 5000 nm. As mentioned in Section 3.1, this is not unreasonable, as the aluminium growth rates are expected to be an overestimate. Some non-uniformity in the epilayer can be observed, possibly due to the mechanical stresses involved in preparing the sample for SEM. The darker lines within the epilayer are due to surface texture on the cleaved face. The thickness
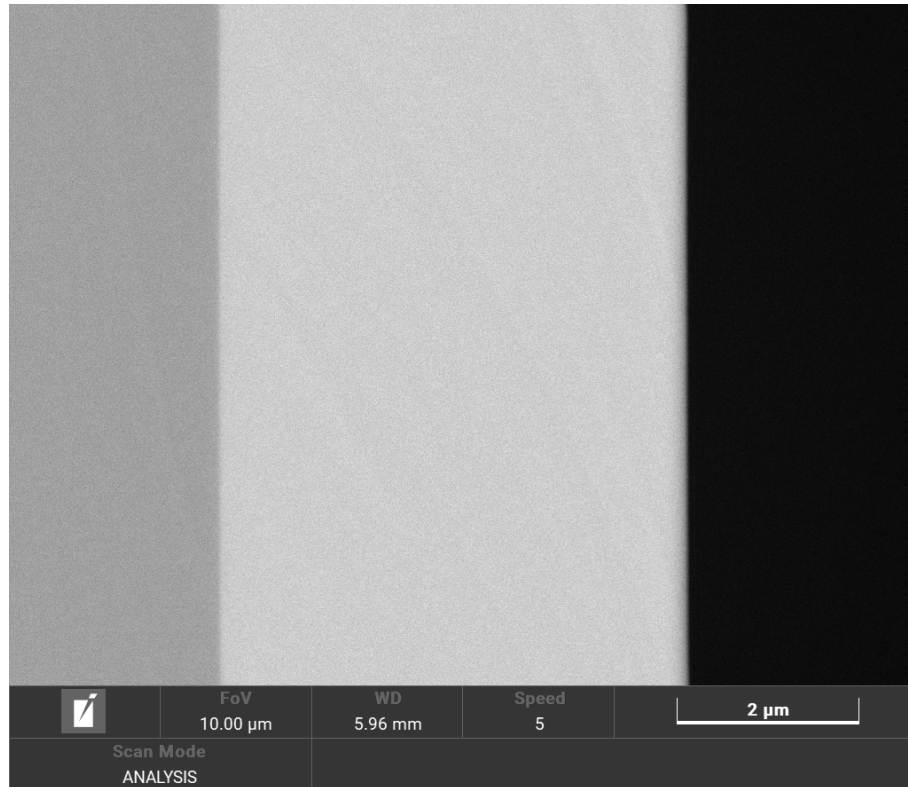
Figure 4.3: Backscatter electron microscopy image of AL1, the first AlAsSb epilayer. Growth direction is right to left. The thickness of the AlAsSb epilayer is 4710±60 nm.

estimate determined through Swanepoel analysis of AL1's reflectance spectra is 4620±50 nm, which is in good agreement with SEM.

The XRD pattern shown in Figure 4.4 indicates the AlAsSb epilayer has an arsenic content of 7.6%. AlAsSb is lattice-matched to GaSb at 300K when As content is approximately 8.5% [30], so a second layer was grown in order to achieve a closer match. Although mismatch is present, it is only slight; the separation between the GaSb and AlAsSb peaks is 158". The periodic fringes to the right of the epilayer peak are due to the presence of the GaSb cap. The minor dimpling effect seen on the substrate peak is due to safety mechanisms on the detector kicking in as incident counts were approaching its operating limit. This reactive attenuation causes the
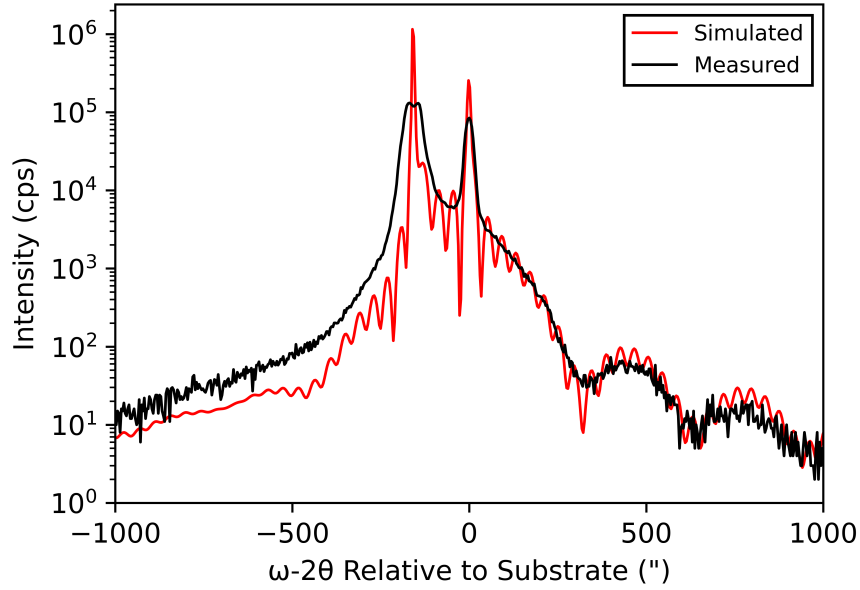
Figure 4.4: XRD pattern of AL1, the first AlAsSb epilayer. The angular separation between the substrate and epilayer peaks is less than 200", so they can be considered approximately lattice-matched. Arsenic content is 7.6%, and the FWHM of the AlAsSb peak is 55".

momentary dip in the centre of the substrate peak where a far sharper peak would be expected. The FWHM of the AlAsSb peak in Figure 4.3 is 55", which implies the material quality is slightly better than that seen in GA1's GaSb layer. This is not necessarily unexpected, as the additional complexities of ternary compound growth are counterbalanced by the similarity between the GaSb and AlAsSb lattice constants.

4.3 AlAsSb Epilayer 2

AL2, the second AlAsSb epilayer, was grown in the same manner as AL1, but on a different wafer of p-doped GaSb substrate. In addition, the GaSb cap was grown to

29

a thickness of only 10 nm, and it remained unaltered. SEM imaging of AL2, shown in Figure 4.5, indicates the sample has high film uniformity. From the SEM image, AL2's thickness is estimated to be 4420±50 nm. The thickness estimate determined through Swanepoel analysis of AL2's reflectance spectra is 4310±60 nm, in good agreement with SEM.
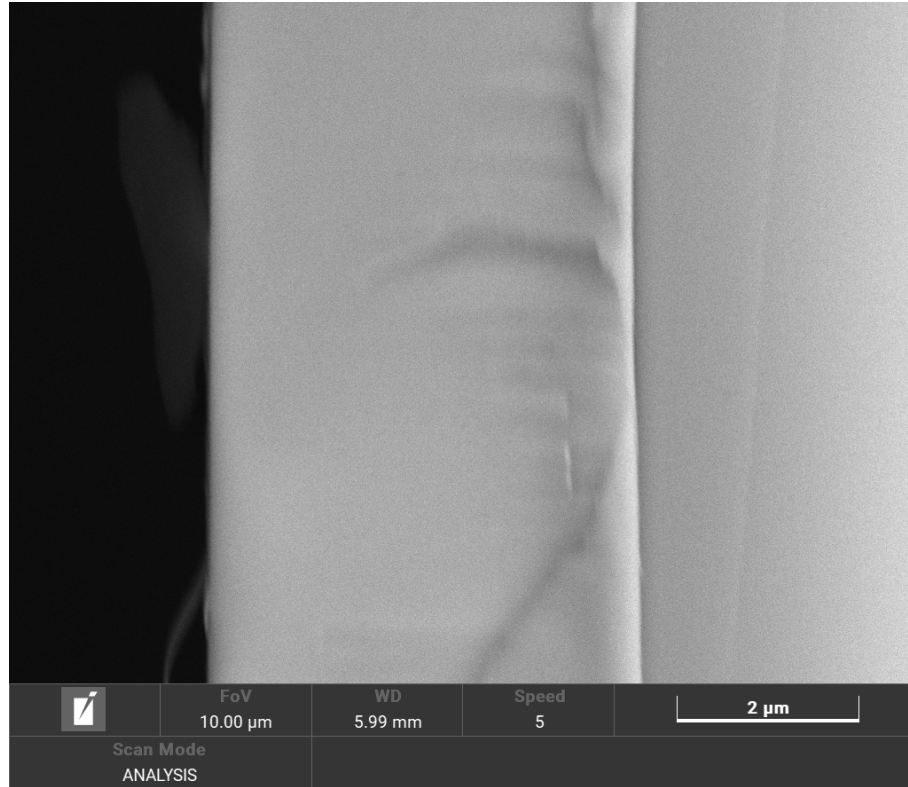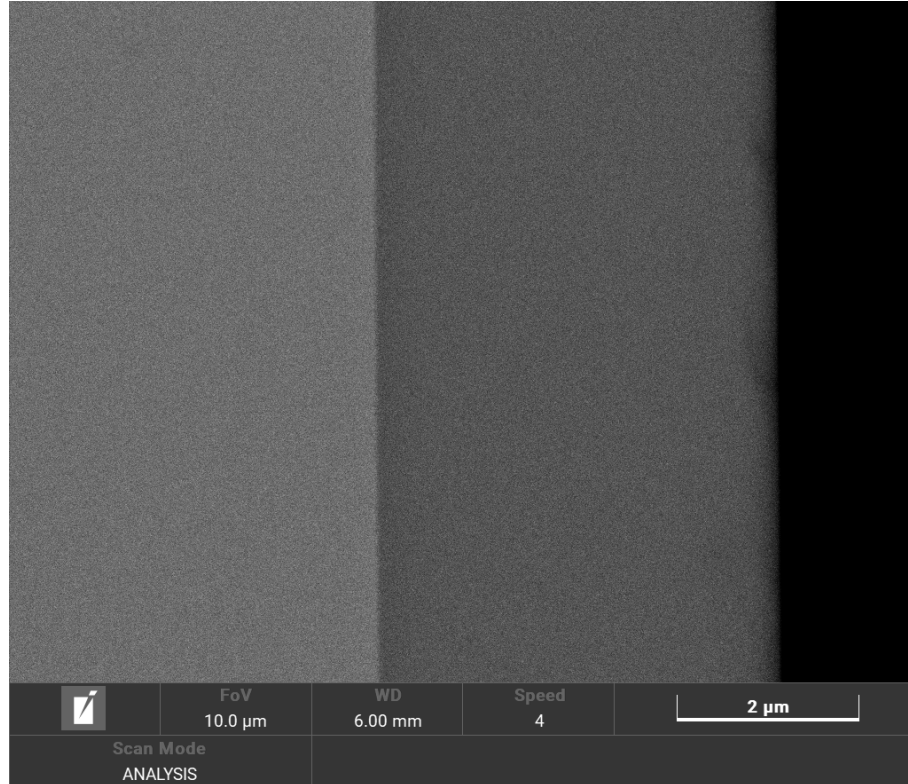

Figure 4.5: Backscatter electron microscopy image of AL2, the second AlAsSb epilayer. Growth direction is left to right. The thickness of the AlAsSb epilayer is 4420±50 nm.

AL2's XRD pattern, shown in Figure 4.6, indicates its arsenic content is 7.4%. The AlAsSb and GaSb peaks are separated by 185", meaning that although the lattice constants are not identical (i.e. some slight mismatch is present), they are within a close enough margin to be considered approximately lattice-matched. The FWHM of the AlAsSb peak in Figure 4.5 is 78", indicating reasonable material quality, although

not as good as GA1 or AL1.
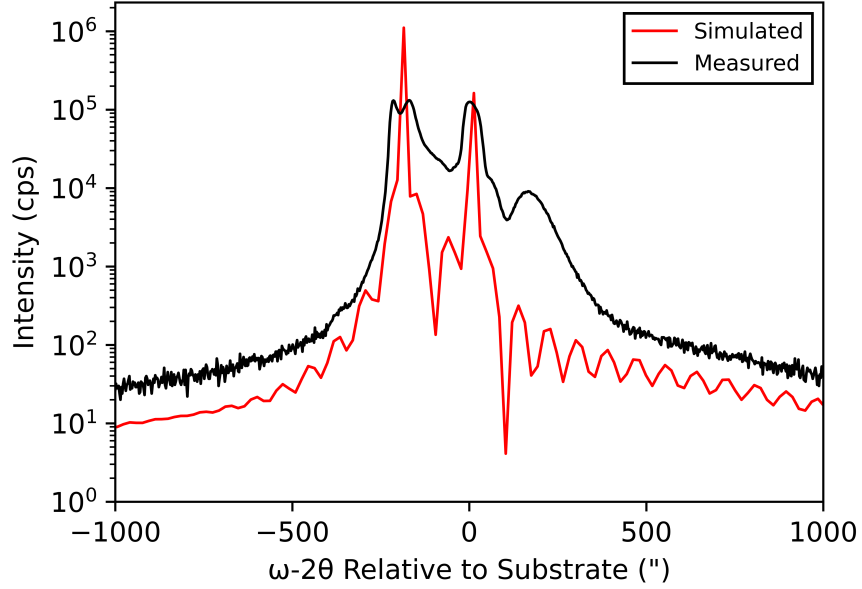
Figure 4.6: XRD pattern of AL2, the second AlAsSb epilayer. The angular separation between the substrate and epilayer peaks is less than 200", so they can be considered approximately lattice-matched. The arsenic content of the AlAsSb epilayer is 7.4%, and the FWHM is 78".

4.4 AlAsSb Epilayer Selection

Since both AL1 and AL2 do not possess the target arsenic content in the AlAsSb layer, the question of which sample to use is not a trivial one: AL1 has less lattice mismatch (158" vs 185") and better material quality (55" vs 78" FWHM), but it was grown with a thicker GaSb cap layer, and despite the cap being etched, it is still thicker than that on AL2 (~18 nm vs 10 nm).

AL2 was selected as the sample for analysis because of its optical simplicity, which is

important for the Swanepoel method, as any additional interfaces can cause distortion in the interference fringes. As an example, a 5000 nm AlAsSb epilayer was grown on GaAs during this study, but the presence of a GaSb buffer layer proved to have too great of an affect on the reflectance fringes for the sample to be usable for the Swanepoel method.

4.5   GaSb/AlAsSb DBR

DBR1 is a 6.5 repeat GaSb/AlAsSb DBR that was grown on the same substrate as AL1 and in the growth run immediately preceding it. The target wavelength for the centre of the stopband was 2100 nm, determined by literature data for the GaSb/AlAsSb refractive indices [12, 13] and calibrated growth rates. The SEM image of DBR1, shown in Figure 4.7, indicates a period thickness of 292 ± 8 nm. The reduced image quality of Figure 4.7 compared to previous SEM imaging is due to conductivity issues during the measurement.

The central peak of DBR1's XRD pattern, shown in Figure 4.8, has a FWHM of 100", which would initially imply slightly lower material quality than expected. Consideration must be given to the fact that the central peak is comprised of both the GaSb and AlAsSb peaks, which would be slightly separated in the case of any mismatch between the layers. The estimated arsenic content in the AlAsSb layers is 8.3%, which means a small amount of lattice mismatch is present, thereby accounting for the broader central peak. The closely-spaced interference fringes are visible in the pattern due to high layer homogeneity; using the period of the fringes, a value of 295 ± 1 nm for the DBR period thickness can be estimated using the fitting tools available in the Bede RADS software.

The proportional thicknesses of GaSb and AlAsSb within DBR1 were determined from
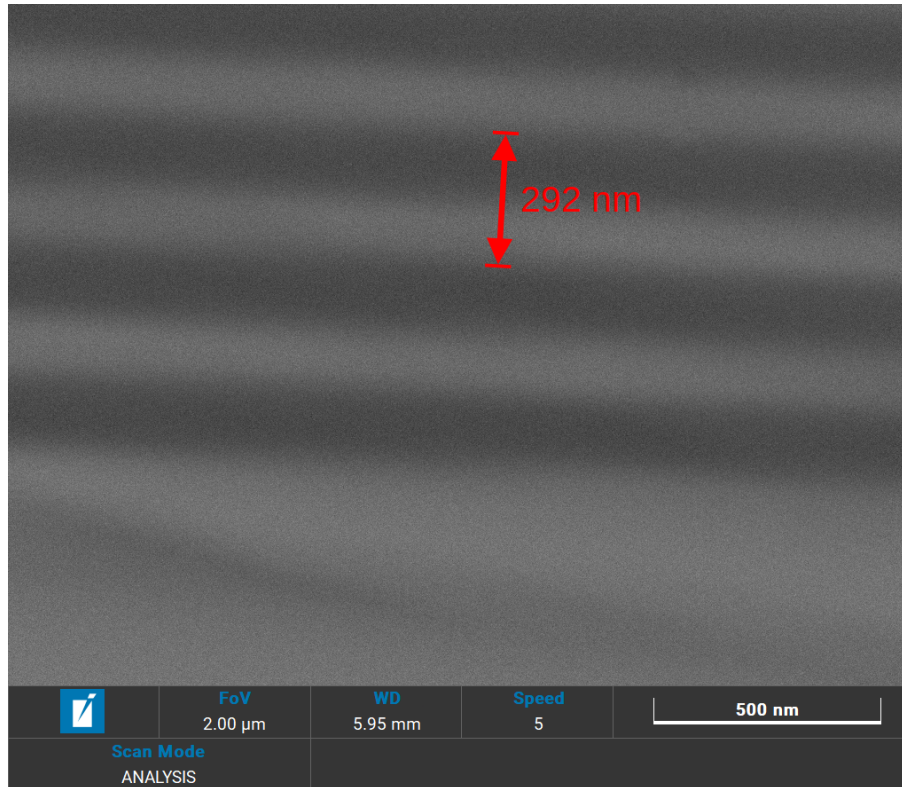
Figure 4.7: Backscatter electron microscopy image of DBR1, the GaSb/AlAsSb DBR. The period thickness of DBR1 is 292±8 nm.

three different sources. The first two used the layer thicknesses from each of AL1 and AL2 to calculate an estimated Al growth rate, and from that, determine the thickness of the AlAsSb layer in the DBR. With the AlAsSb layer thickness known, the thickness of the GaSb was determined by subtraction of the AlAsSb thickness from the 295 nm period thickness. The third method measured the layers as they appear in Figure 4.7 and then scaled those values such that their overall period was equal to 295 nm. The three options each produce similar values, detailed in Table 4.1.
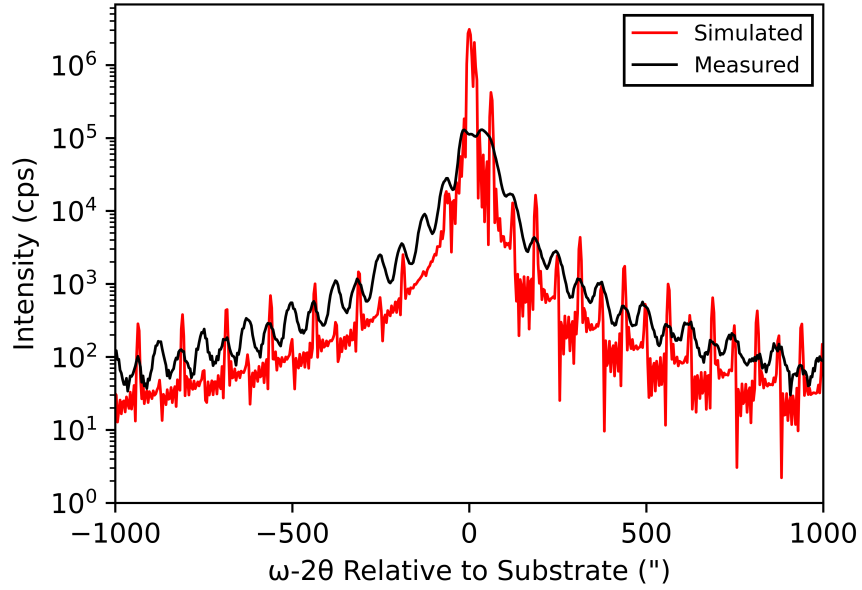
Figure 4.8: XRD pattern of DBR1, a GaSb/AlAsSb DBR.

4.6 Dilute InGaAsSb Epilayers

The InGaAsSb samples studied in Chapter 6 are a set of dilute $(InAs_{0.91}Sb_{0.09})_xGaSb_{1-x}$ epilayers of varying indium content grown on undoped GaAs. The quaternary epilayers were each grown to a target thickness of 1000 nm on top of a GaSb buffer of approximately 500 nm thickness. This sample set is unsuitable for use with the Swanepoel method due to the low epilayer thickness decreasing fringe density and the presence of the buffer layer causing fringe distortions. As a result, the approximated Swanepoel method (outlined in Chapter 6) was applied to them.

Source	AlAsSb Layer (nm)	GaSb Layer (nm)
Original Growth Rates	172.9	138.4
AL1	159.8	135.2
AL2	149.0	146.0
SEM	152.4	142.6

Table 4.1: Thickness estimates of the contrasting layers within DBR1.

Chapter 5

Results II: Dispersive Refractive Indices

The Swanepoel method requires the reflectance spectrum of a film to be measured at both an oblique angle and at normal incidence. Due to the cutoff of the fibre used in the normal incidence setup (Section 3.4), normal incidence reflectance could not be measured at wavelengths longer than 2.4 µm. To circumvent this issue, a method for generating normal incidence reflectance data from oblique measurements was developed. It is detailed herein along with the refractive index values it produced, which are then applied to TMM models of DBR1's stopband.

5.1 Back-extrapolation of Angle-varied Extrema

As described in Section 2.1, increasing the angle of incidence at which light meets a coherent film will shift the spectral positions of the fringe extrema to shorter wavelengths. In a spectral range where refractive index changes minimally due to these wavelength shifts, interference relations may be manipulated to determine

36

normal incidence extremum positions by linear regression.

Swanepoel presents a simple relationship between oblique-angle extremum positions, normal incidence extremum positions, and the angle of incidence which derives from interference conditions, shown in Equation (5.1) [16].

$$n_i{}^2 - sin^2(\theta) = \frac{n_0{}^2 \lambda_i{}^2}{\lambda_0{}^2} \tag{5.1}$$

Symbols are as defined in Section 2.1, with the addition of θ as the angle of incidence. Equation (5.1) can be rearranged to obtain Equation (5.2).

$$\lambda_i{}^2 = \lambda_0{}^2 \frac{n_i{}^2}{n_0{}^2} - \frac{\lambda_0{}^2}{n_0{}^2} sin^2\theta \tag{5.2}$$

Under the assumption that the fringes are in a low-dispersion region, and thus $n_i \approx n_0 \approx n$, Equation (5.3) can be formed.

$$\lambda_i{}^2 = \lambda_0{}^2 - \frac{\lambda_0{}^2}{n^2} sin^2\theta \tag{5.3}$$

This allows the retrieval of the normal incidence position of a given extremum from a plot of the square of the oblique incidence positions against the square of the sine of the oblique angle. An example of this, using data from GA1, is shown in Figure 5.1.

The experimental data was taken from GA1 in 5° increments across the 30-55° range. The simulated data was produced using TMM modelling of GaSb and GaAs refractive index data [17, 11]. The shift in intercept between the simulated and real data series can be accounted for by a small difference in the thickness of the sample compared to what was simulated. A small change in layer thickness can shift the position of an extremum, causing extrema of the same order to appear at different wavelengths
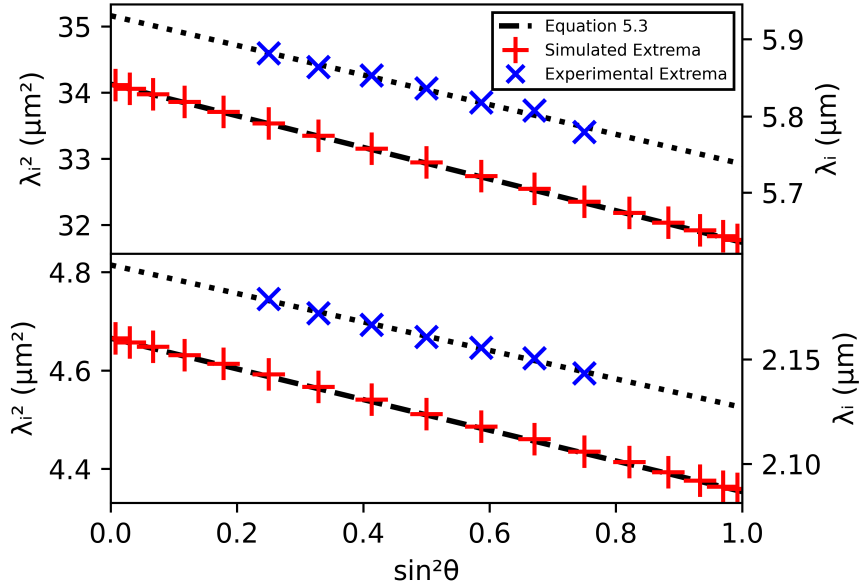
Figure 5.1: Example back-extrapolation plot for the determination of normal incidence extrema from oblique measurements. The dotted line is a linear regression for the experimental data, which was measured from GA1. The simulated extrema have been modelled using TMM with literature data [11, 17].

between the simulation and experimental data.

The agreement between the extremum positions and the lines that fit them indicate that the $n_i \approx n_0 \approx n$ approximation is valid in the wavelength regions studied. The similarity in gradient between simulation and experiment indicates that despite the slight difference in offset, experimental refractive index should be close to literature data [11] at the wavelengths studied.

Uncertainty in the linear regression propagates trivially to uncertainties in the extremum positions calculated from it but propagation of those errors into uncertainties in the MCE fitting parameters bears consideration. The uncertainty in each extremum's position is treated as the standard deviation in a normal distribution that

has a mean value equal to the extremum position. Samples are taken from each extremum's normal distribution to create a set of "noisy" data. The "noisy" data is then processed through the standard Swanepoel method. This process is run 16 times, with "noisy" data re-sampled each time, to generate a data set of noise-affected values for the MCE parameters. With that dataset generated, standard errors in each MCE parameter are then calculated. That process is performed 20 times to allow for the calculation of mean standard errors in each MCE parameter due to linear regression uncertainty.

5.2 GaSb Dispersive Refractive Index

Using the linear regression method outlined above on variable angle reflectance data taken from GA1, MCE coefficients for GaSb were calculated. The coefficients are presented in Table 5.1 and the resulting dispersion curve is shown in Figure 5.2.

Parameter	a (nm^x)	b	x
Value	$(7.7 \pm 0.2) \times 10^9$	14.3 ± 0.4	3.009 ± 0.002

Table 5.1: MCE (Equation (2.3)) fitting parameters for GaSb.

The refractive index presented for GaSb is in clear agreement with literature data [11, 12, 14], and does not serve to highlight any substantial discrepancy or issue with existing values; the primary appeal of the data presented here is its coverage of the full 2-8 μm range. The strength of the agreement with literature data does indicate that the uncertainty for the presented dispersion curve is overly-conservative. However, the size of the uncertainty should be viewed in the context that error regions on dispersion curves are not seen in literature, so there is no solid reference for comparison to determine whether the uncertainty estimate is reasonable.
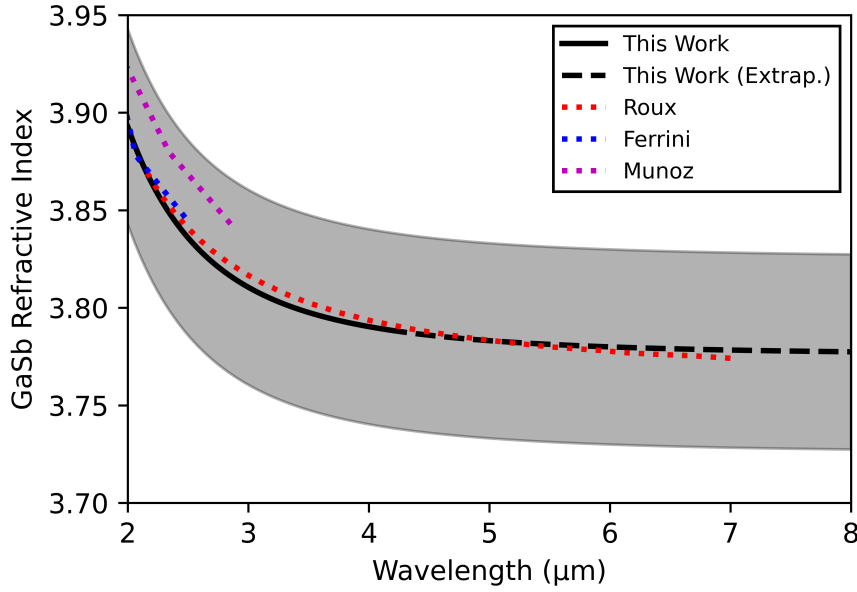
Figure 5.2: Dispersive refractive index of GaSb compared to literature data [11, 12, 14]. The shaded region indicates the uncertainty in the presented value. The solid black line indicates the range over which reflectance was directly measured, the dashed region is a extrapolation of the model into the transparent region.

5.3 AlAsSb Dispersive Refractive Index

Using the linear regression method outlined above on variable angle reflectance data taken from AL2, MCE coefficients for $AlAs_{0.074}Sb$ were calculated. The coefficients are presented in Table 5.2 and the resulting dispersion curve is shown in Figure 5.3. The curve is also placed into greater context with bounding values in Figure 5.4.

Parameter	a (nm^x)	b	x
Value	$(1.02 \pm 0.03) \times 10^{10}$	10.2 ± 0.2	3.221 ± 0.007

**Table 5.2:** MCE (Equation (2.3)) fitting parameters for AlAsSb.
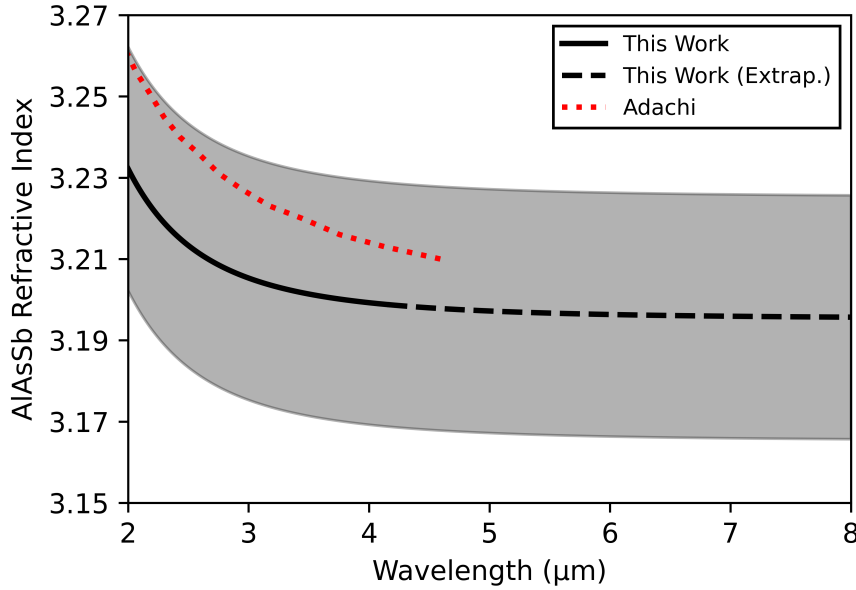
Figure 5.3: Dispersive refractive index of AlAs$_{0.074}$Sb, compared to literature data [30]. The shaded region indicates the uncertainty in the presented value. The solid black line indicates the range over which reflectance was directly measured, the dashed region is a extrapolation of the model into the transparent region.

Figure 5.3 clearly shows that the dispersion curve presented for AlAs$_{0.074}$Sb is in reasonable agreement with simulated literature data [30].

In context, this work's value for the AlAs$_{0.074}$Sb dispersive refractive index can be seen to lie comfortably within the bounds set by AlSb [32] and AlAs [33] literature data. The approximation in Figure 5.4 was produced by a Vegard's Law-style [34] linear interpolation of the aforementioned literature values for AlSb and AlAs refractive indices. The discrepancy between this work's curve and the approximation is mirrored by the discrepancy between the approximation and simulated literature data [30], implying that the behaviour of AlAs$_x$Sb refractive index may not be simply linear with respect to Arsenic content. The experimental reference data shown is extrapolated

41
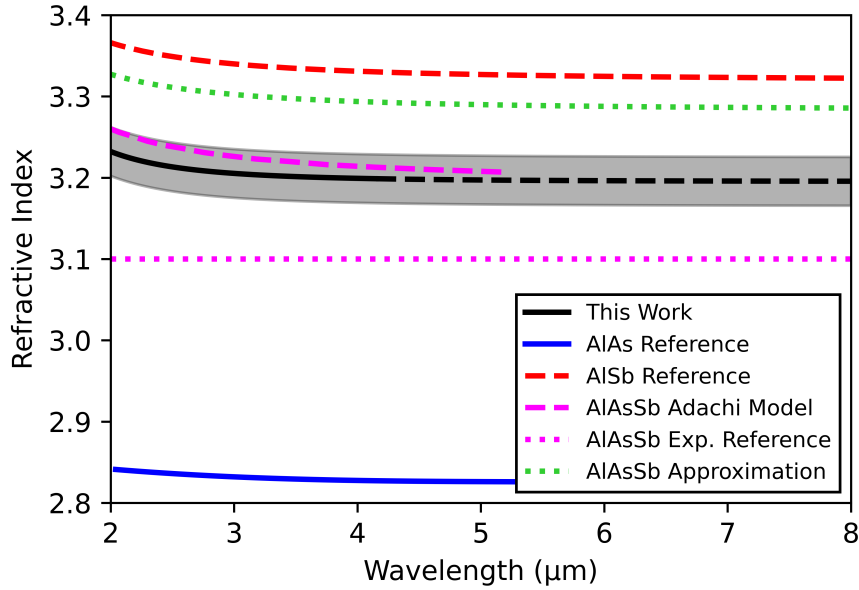
Figure 5.4: Dispersive refractive index of AlAsSb lattice matched to GaSb, compared to literature data [13, 30] and an approximation of the expected value, bounded by literature data for AlSb and AlAs [32, 33]. The shaded region indicates the uncertainty in the presented value. The solid black line indicates the range over which reflectance was directly measured, the dashed region is a extrapolation of the model into the transparent region.

from shorter wavelength data [13]. The discrepancy between this work's curve and the shorter-wavelength experimental reference data is harder to account for, although the significant difference in methodology is worth noting.

5.4 Applications to DBR Analysis

To evaluate the accuracy and utility of the dispersive refractive indices presented above, they were applied to TMM modelling of DBR1's stopband. The results of

the modelling are compared to literature data and the normal incidence reflectance measurement of DBR1.
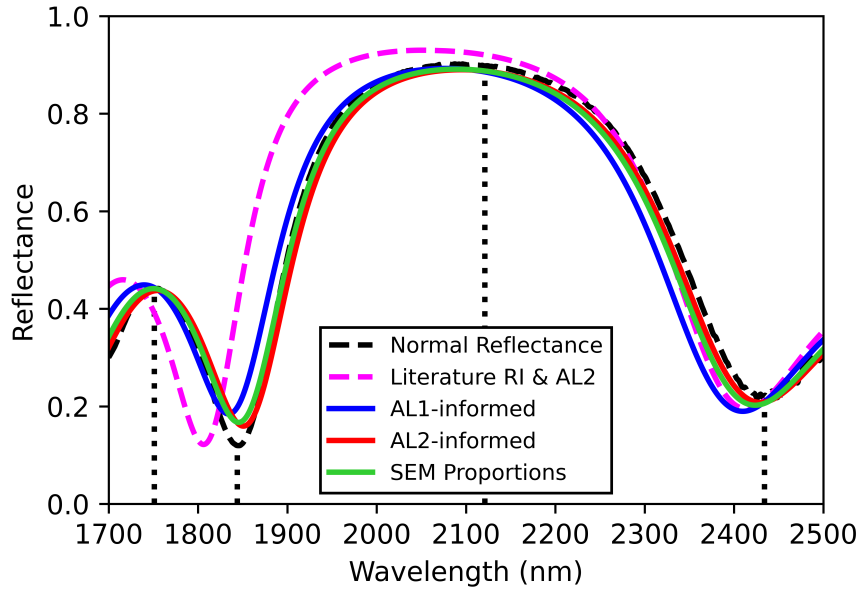
Figure 5.5: DBR1 stopband modelled using TMM. Refractive indices for the GaSb and AlAsSb layers are taken from Figure 5.2 and Figure 5.3 respectively. Layer thicknesses are taken from Table 4.1. Experimental literature data is used for comparison [13, 12]

To determine which of the value pairs for DBR1's layer thicknesses presented in Table 4.1 are most accurate, they are compared in Figure 5.5 to the measured normal incidence reflectance of DBR1, clearly showing the stopband centred around 2100 nm, as expected. Each pair of values agrees closely with the experimentally measured stopband shape, however the AL2-informed values are the closest.

To evaluate the impact of the uncertainties in the refractive index values presented in Figures 5.2 and 5.3, Figure 5.6 accounts for increase or decrease in contrast and its affects on the stopband position and shape. Layer thicknesses are taken to be

the AL2-informed values from Table 4.1. Both reference lines use Ferrini's GaSb data [12].
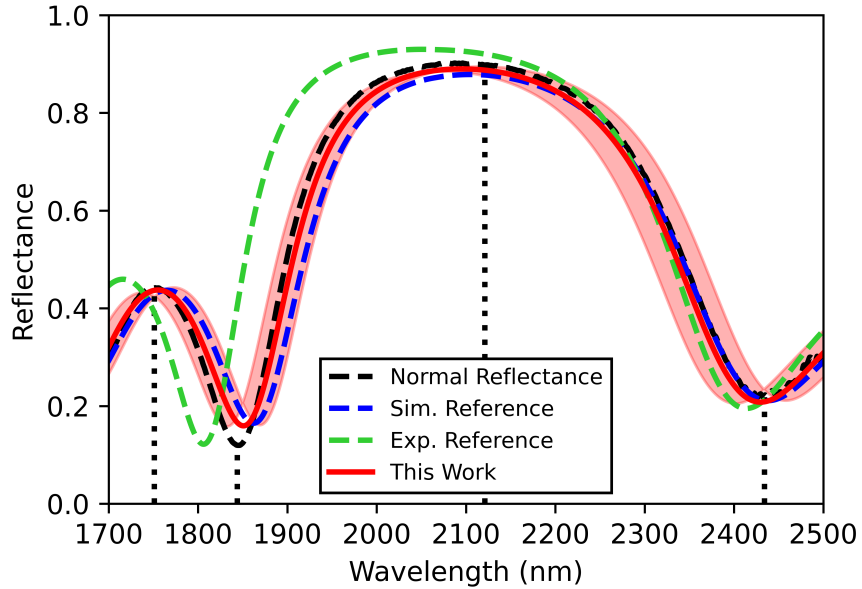
Figure 5.6: DBR1 stopband modelled using TMM. The shaded region indicates the uncertainty in stopband position caused by refractive index uncertainties. Experimental reference data takes AlAsSb RI from Saadallah [13], simulated reference data uses Adachi's AlAsSb values [30]. Reference data for GaSb is sourced from Ferrini [12].

Upon review, the uncertainties presented in Figures 5.2 and 5.3 seem appropriate, if a little conservative - the range in stopband values they cause does not seem disproportionate to the data's agreement with the measured reflectance.

Figure 5.6 illustrates well the improvement over literature data offered by the dispersive refractive indices presented in Figure 5.2 and Figure 5.3. The stopband simulated using this work's data shows closer agreement with experimentally measured reflectance than both experimental and simulated literature data. In addition,

the refractive indices presented in this work cover the 2-8 µm range completely, unlike experimental literature values, offering greater utility for the modelling of GaSb-based cavity devices.

Chapter 6

Results III: Static Refractive Indices

A different method for circumventing the Swanepoel method's reliance on normal incidence reflection is presented herein. Much like the linear regression method detailed in Section 3.3, this method analyses experimentally measured reflectance spectra of coherent films at variable angles, but does not use the Swanepoel method beyond its mathematical underpinning.

6.1 Approximation of the Swanepoel Method

Using the interference fringe relations given in Section 2.1, it is possible to construct the relation shown in Equation (6.1).

$$\frac{n_1 \cos{(r_1)}}{\lambda_1} = \frac{n_2 \cos{(r_2)}}{\lambda_2} \tag{6.1}$$

Assuming the incident medium is air, Snell's Law in the form $n_1 \sin{(r_1)} = \sin{(\theta_1)}$ may be used to rearrange Equation (6.1) into Equation (6.2).

$$\frac{n_1{}^2 - sin^2\,(\theta_1)}{\lambda_1{}^2} = \frac{n_2{}^2 - sin^2\,(\theta_2)}{\lambda_2{}^2} \tag{6.2}$$

The relation between n_1 and n_2 may be approximated by a Taylor expansion of the MCE, shown in Equation (6.3).

$$n_2{}^2 \approx n_1{}^2 + \frac{ax\,(\lambda_1 - \lambda_2)}{\lambda_1{}^{x+1}} \tag{6.3}$$

Equation (2.3) and Equation (6.3) may then be substituted into Equation (6.2) and rearranged in order to retrieve Equation (6.4).

$$\frac{a}{\lambda_1{}^x} + b = \frac{ax\lambda_1{}^3 + \lambda_1{}^{x+1}\lambda_2{}^2\,sin^2\,(\theta_1) - \lambda_1{}^{x+1}\lambda_1{}^2\,sin^2\,(\theta_2) - ax\lambda_1{}^2\lambda_2}{\lambda_1{}^{x+1}\,\left(\lambda_2{}^2 - \lambda_1{}^2\right)} \tag{6.4}$$

Linear regression can then be used with Equation (6.4) to retrieve parameters a, b, and x. This method fits the *x* parameter of the Cauchy-like model very sensitively, so its scope is limited to calculations of non-dispersive refractive index. However, its use of each possible unique extremum pair allows for the retrieval of the parameters for the Cauchy-like model from very few extrema. This is most useful in the case of thinner epilayers that may be available where samples were not able to be grown specifically for the linear regression method outlined previously. A further disadvantage of this approximated method is that it does not retrieve an estimate for the epilayer thickness, which can be very useful in some cases.

6.2   Long-wavelength Refractive Index of InGaAsSb

Despite the limitations of the approximated Swanepoel method, it is shown in Figure 6.1 to be capable of accurately resolving trends in the refractive index of

dilute $(InAs_{0.91}Sb_{0.09})_xGaSb_{1-x}$, despite the magnitude of the non-dispersive refractive indices being offset from expected values slightly.
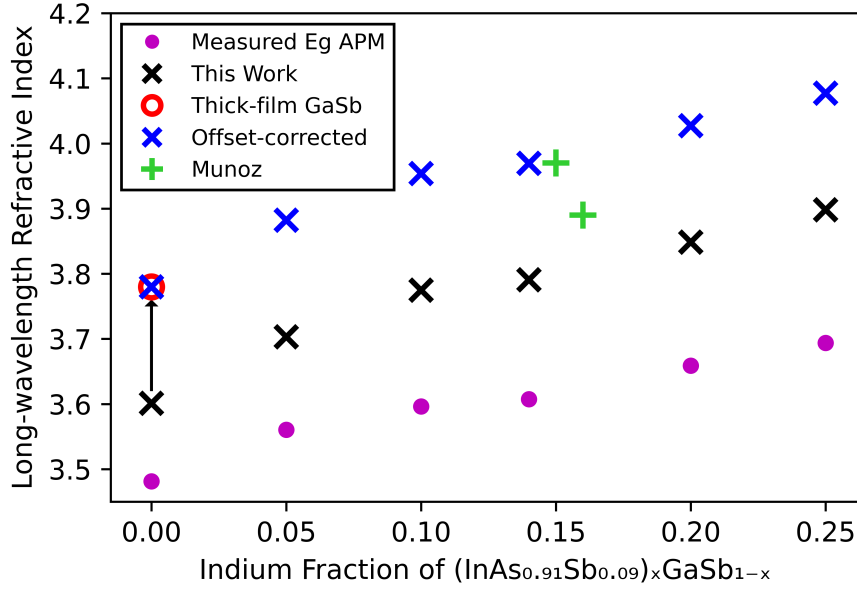
Figure 6.1: Non-dispersive infrared refractive index of $(InAs_{0.91}Sb_{0.09})_xGaSb_{1-x}$ alloy is plotted against indium fraction, x. Literature data [15] and the APM are provided for comparison.

The APM values shown in Figure 6.1 are calculated using experimental measurements of the optical bandgaps for these samples detailed in a previous study [35]. The offset between the APM and the values returned by the approximated Swanepoel method can be accounted for in the tendency of the APM to underestimate the refractive indices of gallium-rich compounds. The offset correction is performed simply by matching the x=0 value for the alloy to the GaSb data presented in Section 5.2. The offset-corrected values are in fair agreement with the magnitude of the limited literature data available [15].

Overall, the approximated Swanepoel method (once offset-corrected) is shown to be

capable of matching both expected RI trends with indium fraction and the magnitude of refractive index quite well. The method's capability to resolve subtle differences in RI is shown most clearly by it replicating the lower gradient between indium fractions of 0.1 and 0.14 that is present in the APM values. The lower gradient is derived from slight changes in the optical bandgap of the samples due to composition imperfections; Figure 6.1 demonstrates that the approximated Swanepoel method is capable of resolving small changes in RI caused by these small composition variations. The work presented throughout this chapter offers a potentially valuable alternative to the standard Swanepoel method in the likely case where bespoke epilayers for use with the variable angle linear regression method are unavailable or impractical.

Chapter 7

Conclusion & Further Work

This study has successfully met its objective of developing methods for the use of the Swanepoel method without reliance on normal incidence reflectance spectra. The variable angle linear regression method has produced dispersive refractive index data that is in close accordance with existing values whilst extending beyond the wavelength range studied in literature (Chapter 5). The modified Cauchy equation (Equation (2.3)) parameters for GaSb were determined to be $(7.7 \pm 0.2) \times 10^9$ nm^x, 14.3 ± 0.4, and 3.009 ± 0.002. The parameters found for AlAsSb were $(1.02 \pm 0.03) \times 10^{10}$ nm^x, 10.2 ± 0.2, and 3.221 ± 0.007. Where bespoke epilayers for the aforementioned method are unavailable, the approximated Swanepoel method has been shown to predict a reasonable increase of 0.30 in non-dispersive infrared refractive indices for InGaAsSb as Indium content increases from 0 to 25% (Chapter 6), and the presented values are in fair agreement with literature.

The methodology presented for the measurement of variable angle reflectance spectra is the most complete and developed procedure as of yet in Dr Marshall's research group, and the estimate of the variable reflector's angular uncertainty is a new value which is expected to have lasting utility. Furthermore, the optimisations

made to the measurement procedure have improved the time efficacy of data collection which offers additional long-term benefit to the group.

Analysis of variable angle reflectance spectra by linear regression offers a promising new method for laboratories not equipped for broad-spectrum normal incidence measurement to make use of the Swanepoel method or measure other interference-derived spectral features on samples. The dispersive refractive indices for GaSb and AlAsSb produced from this method represent an improvement on existing data in terms of utility; the 2-8 µm range is highly used by GaSb-based cavity devices and the data presented in this dissertation is complete over that range, unlike literature values.

The presented dispersive refractive indices have shown improvements over literature values when applied to TMM modelling of DBR stopbands. Modelling using the data shown in this work will allow for more precise designing of new cavity devices, to an extent that would have been problematic with modelling based on existing experimental data. Literature data use in TMM modelling had allowed GaSb-based cavity design in Dr Marshall's group to progress to a point where discrepancies between model and experiment data had most frequently been attributed to small thickness or experimental errors. The new data allows for progression towards highly selective devices, where stopband alignment is especially important, and it is likely to be useful in supporting commercialisation efforts.

7.1   Future Work

Although the study detailed in this dissertation has been broadly successful, the tight time constraint has left multiple avenues open for further investigation. Improvement could be made to the theoretical underpinning of the work by replicating existing

efforts [22] to implement the Sellmeier model into the Swanepoel method to allow for better modelling of dispersive refractive indices in regions where dispersion is more significant.

On the experimental side, extensions up to 8 µm in the wavelength range of extrema studied would help reinforce the validity of the data presented, but removing the effect of atmospheric absorption will be non-trivial due to the Swanepoel method's reliance on a continuous series of extrema. One way to achieve this would be to refine the peak-finding algorithm used in this work to allow for discrimination between interference fringe extrema and extrema caused by atmospheric absorption. Additionally, the VERTEX 70 allows for the sample chamber to be purged using nitrogen gas, which would suppress, if not entirely eliminate, the presence of atmospheric absorption-derived extrema.

Considering more dramatic changes in apparatus, the atmospheric issues could be entirely eliminated if the measurements were performed under vacuum. Furthermore, if the reflectance measurement environment was connected with the MBE growth chamber under vacuum, the AlAsSb samples could be grown without a GaSb cap, allowing for an optically simpler epilayer of the material to be studied. Short of this, a re-growth of the AlAsSb epilayers with optimised growth conditions such that the resultant As content is 8.5% would better justify the application of the measured dispersive refractive index to lattice-matched DBRs. Finally, a more complete assessment of error propagation through the variable angle linear regression method would allow for more accurate error bounds to be assigned to the dispersive refractive indices produced from it.

References

[1] Alex M. Green et al. "Resonant-cavity-enhanced photodetectors and LEDs in the mid-infrared". In: *Physica E: Low-dimensional Systems and Nanostructures* 20.3 (2004). Proceedings of the 11th International Conference on Narrow Gap Semiconductors, pp. 531–535. ISSN: 1386-9477. DOI: `https://doi.org/10.1016/j.physe.2003.09.004`.

[2] Laura Hanks et al. "Quasi-planar InGaAsSb p-B-n photodiodes for spectroscopic sensing". In: *Optics Express* 31 (Apr. 2023), p. 14358. DOI: `10.1364/OE.485631`.

[3] T. N. Danilova et al. "Light-emitting diodes based on GaSb alloys for the 1.6–4.4 μm mid-infrared spectral range". In: *Semiconductors* 39.11 (Nov. 2005), pp. 1235–1266. ISSN: 1090-6479. DOI: `10.1134/1.2128447`.

[4] Eungbeom Yeon et al. "Reduction of Structural Defects in the GaSb Buffer Layer on (001) GaP/Si for High Performance InGaSb/GaSb Quantum Well Light-Emitting Diodes". In: *ACS Applied Materials & Interfaces* 15.48 (Dec. 2023), pp. 55965–55974. ISSN: 1944-8244. DOI: `10.1021/acsami.3c10979`.

[5] A. P. Craig et al. "Resonant cavity enhanced photodiodes on GaSb for the midwave infrared". In: *Applied Physics Letters* 114.15 (Apr. 2019), p. 151107. ISSN: 0003-6951. DOI: `10.1063/1.5082895`.

[6]   Furat A. Al-Saymari et al. "Mid-infrared resonant cavity light emitting diodes operating at 4.5 μm". In: *Opt. Express* 28.16 (Aug. 2020), pp. 23338–23353. DOI: 10.1364/OE.396928.

[7]   V. Letka et al. "A superlattice-based resonant cavity-enhanced photodetector operating in the long-wavelength infrared". In: *Applied Physics Letters* 117.7 (Aug. 2020), p. 073503. ISSN: 0003-6951. DOI: 10.1063/5.0013553.

[8]   Jian Feng et al. "Self-Mode-Locked 2-μm GaSb-Based Optically Pumped Semiconductor Disk Laser". In: *Applied Sciences* 13.12 (2023). ISSN: 2076-3417. DOI: 10.3390/app13126873.

[9]   Pengchong Li et al. "Optimization design and preparation of near ultraviolet AlGaN/GaN distributed Bragg reflectors". In: *Superlattices and Microstructures* 122 (2018), pp. 661–666. ISSN: 0749-6036. DOI: https://doi.org/10.1016/j.spmi.2018.05.034.

[10]   C J R Sheppard. "Approximate calculation of the reflection coefficient from a stratified medium". In: *Pure and Applied Optics: Journal of the European Optical Society Part A* 4.5 (Sept. 1995), p. 665. DOI: 10.1088/0963-9659/4/5/018.

[11]   S. Roux et al. "Mid-infrared characterization of refractive indices and propagation losses in GaSb/AlXGa1-XAsSb waveguides". In: *Applied Physics Letters* 107.17 (Oct. 2015), p. 171901. ISSN: 0003-6951. DOI: 10.1063/1.4934702. eprint: https://pubs.aip.org/aip/apl/article-pdf/doi/10.1063/1.4934702/13148559/171901_1_online.pdf.

[12]   R. Ferrini, M. Patrini, and S. Franchi. "Optical functions from 0.02 to 6 eV of AlxGa1-xSb/GaSb epitaxial layers". In: *Journal of Applied Physics* 84.8 (Oct. 1998), pp. 4517–4524. ISSN: 0021-8979. DOI: 10.1063/1.368677. eprint: https://pubs.aip.org/aip/jap/article-pdf/84/8/4517/19242013/4517_1_online.pdf.

[13] Faycel Saadallah et al. "Photothermal investigations of thermal and optical properties of GaAlAsSb and AlAsSb thin layers". In: *Journal of Applied Physics* 94.8 (Oct. 2003), pp. 5041–5048. ISSN: 0021-8979. DOI: 10.1063/1.1611290. eprint: https://pubs.aip.org/aip/jap/article-pdf/94/8/5041/18705201/5041_1_online.pdf.

[14] M. Muñoz et al. "Spectral ellipsometry of GaSb: Experiment and modeling". In: *Physical Review B* 60 (Sept. 1999). DOI: 10.1103/PhysRevB.60.8105.

[15] M. Muñoz et al. "Optical constants of Ga1-xInxAsySb1-y lattice matched to GaSb (001): Experiment and modeling". In: *Journal of Applied Physics* 87.4 (Feb. 2000), pp. 1780–1787. ISSN: 0021-8979. DOI: 10.1063/1.372092. eprint: https://pubs.aip.org/aip/jap/article-pdf/87/4/1780/18979717/1780_1_online.pdf.

[16] R. Swanepoel. "Determining refractive index and thickness of thin films from wavelength measurements only". In: *J. Opt. Soc. Am. A* 2.8 (Aug. 1985), pp. 1339–1343. DOI: 10.1364/JOSAA.2.001339.

[17] Lukas W. Perner et al. "Simultaneous measurement of mid-infrared refractive indices in thin-film heterostructures: Methodology and results for GaAs/AlGaAs". In: *Phys. Rev. Res.* 5 (3 July 2023), p. 033048. DOI: 10.1103/PhysRevResearch.5.033048.

[18] Timo Gissibl et al. "Refractive index measurements of photo-resists for three-dimensional direct laser writing". In: *Opt. Mater. Express* 7.7 (July 2017), pp. 2293–2298. DOI: 10.1364/OME.7.002293.

[19] Omer Akpinar et al. "Swanepoel method for AlInN/AlN HEMTs". In: *Journal of Materials Science: Materials in Electronics* 31.13 (July 2020), pp. 9969–9973. ISSN: 1573-482X. DOI: 10.1007/s10854-020-03590-6.

[20] Ion Tirca et al. "Refractive index of WO3 thin films grown under various temperatures determined by the Swanepoel method". In: *Physica B: Condensed*

Matter 620 (2021), p. 413266. ISSN: 0921-4526. DOI: `https://doi.org/10.1016/j.physb.2021.413266`.

[21] J. Sánchez-González et al. "Determination of optical properties in nanostructured thin films using the Swanepoel method". In: *Applied Surface Science* 252.17 (2006), pp. 6013–6017. ISSN: 0169-4332. DOI: `https://doi.org/10.1016/j.apsusc.2005.11.009`.

[22] Y. Fang et al. "Determining the refractive index dispersion and thickness of hot-pressed chalcogenide thin films from an improved Swanepoel method". In: *Optical and Quantum Electronics* 49.7 (June 2017), p. 237. ISSN: 1572-817X. DOI: `10.1007/s11082-017-1057-9`.

[23] Youliang Jin et al. "Improvement of Swanepoel method for deriving the thickness and the optical properties of chalcogenide thin films". In: *Opt. Express* 25.1 (Jan. 2017), pp. 440–451. DOI: `10.1364/OE.25.000440`.

[24] T S Moss. "A Relationship between the Refractive Index and the Infra-Red Threshold of Sensitivity for Photoconductors". In: *Proceedings of the Physical Society. Section B* 63.3 (Mar. 1950), p. 167. DOI: `10.1088/0370-1301/63/3/302`.

[25] David R. Penn. "Wave-number-dependent dielectric function of semiconductors". In: *Physical Review* 128.5 (1962). Cited by: 2197, pp. 2093–2097. DOI: `10.1103/PhysRev.128.2093`.

[26] V. P. Gupta and N. M. Ravindra. "Comments on the Moss Formula". English (US). In: *physica status solidi (b)* 100.2 (Aug. 1980), pp. 715–719. ISSN: 0370-1972. DOI: `10.1002/pssb.2221000240`.

[27] Steven J. Byrnes. *Multilayer optical calculations*. 2020. arXiv: `1603.02720` `[physics.comp-ph]`. URL: `https://arxiv.org/abs/1603.02720`.

[28] Lisha C. Lohithakshan, Vishnu Geetha, and Pradeesh Kannan. "Single polymer-variable index for the design and fabrication of variable stop band distributed

Bragg reflectors". In: *Optical Materials* 110 (2020), p. 110509. ISSN: 0925-3467. DOI: https://doi.org/10.1016/j.optmat.2020.110509.

[29] J. D. Hunter. "Matplotlib: A 2D graphics environment". In: *Computing in Science & Engineering* 9.3 (2007), pp. 90–95. DOI: 10.1109/MCSE.2007.55.

[30] Sadao Adachi. "Band gaps and refractive indices of AlGaAsSb, GaInAsSb, and InPAsSb: Key properties for a variety of the 2–4-μm optoelectronic device applications". In: *Journal of Applied Physics* 61.10 (May 1987), pp. 4869–4876. ISSN: 0021-8979. DOI: 10.1063/1.338352. eprint: https://pubs.aip.org/aip/jap/article-pdf/61/10/4869/18610987/4869_1_online.pdf. URL: https://doi.org/10.1063/1.338352.

[31] Charles J. Reyner et al. "Characterization of GaSb/GaAs interfacial misfit arrays using x-ray diffraction". In: *Applied Physics Letters* 99.23 (Dec. 2011), p. 231906. ISSN: 0003-6951. DOI: 10.1063/1.3666234. eprint: https://pubs.aip.org/aip/apl/article-pdf/doi/10.1063/1.3666234/14461254/231906_1_online.pdf.

[32] A. B. Djurišić et al. "Modeling the optical properties of AlSb, GaSb, and InSb". In: *Applied Physics A* 70.1 (Jan. 2000), pp. 29–32. ISSN: 1432-0630. DOI: 10.1007/s003390050006.

[33] C Palmer et al. "Mid-infrared (λ 2–6 μm) measurements of the refractive indices of GaAs and AlAs". In: *Semiconductor Science and Technology* 17.11 (Oct. 2002), p. 1189. DOI: 10.1088/0268-1242/17/11/310.

[34] L. Vegard. "Die Konstitution der Mischkristalle und die Raumfüllung der Atome". In: *Zeitschrift für Physik* 5.1 (Jan. 1921), pp. 17–26. ISSN: 0044-3328. DOI: 10.1007/BF01349680.

[35] K Mamić et al. "Electrical and optical characterisation of InGaAsSb-based photodetectors for SWIR applications". In: *Semiconductor Science and Technology* 39.11 (Sept. 2024), p. 115002. DOI: 10.1088/1361-6641/ad7a21.